SIAM Review
Vol. 54, No. 4, pp. 757–798

Filtering Deterministic Layer Effects in Imaging*

L. Borcea†
F. González del Cueto‡
G. Papanicolaou§
C. Tsogka¶

Abstract. Sensor array imaging arises in applications such as nondestructive evaluation of materials with ultrasonic waves, seismic exploration, and radar. The sensors probe a medium with signals and record the resulting echoes, which are then processed to determine the location and reflectivity of remote reflectors. These could be defects in materials such as voids, fault lines or salt bodies in the earth, and cars, buildings, or aircraft in radar applications. Imaging is relatively well understood when the medium through which the signals propagate is smooth, and therefore nonscattering. But in many problems the medium is heterogeneous, with numerous small inhomogeneities that scatter the waves. We refer to the collection of inhomogeneities as clutter, which introduces an uncertainty in imaging because it is unknown and impossible to estimate in detail. We model the clutter as a random process. The array data is measured in one realization of the random medium, and the challenge is to mitigate cumulative clutter scattering so as to obtain robust images that are statistically stable with respect to different realizations of the inhomogeneities.

Scatterers that are not buried too deep in clutter can be imaged reliably with the coherent interferometric (CINT) approach. But in heavy clutter the signal-to-noise ratio (SNR) is low and CINT alone does not work. The "signal," the echoes from the scatterers to be imaged, is overwhelmed by the "noise," the strong clutter reverberations. There are two existing approaches for imaging at low SNR: The first operates under the premise that data are incoherent so that only the intensity of the scattered field can be used. The unknown coherent scatterers that we want to image are modeled as changes in the coefficients of diffusion or radiative transport equations satisfied by the intensities, and the problem becomes one of parameter estimation. Because the estimation is severely ill-posed, the results have poor resolution, unless very good prior information is available and large arrays are used. The second approach recognizes that if there is some residual coherence in the data, that is, some reliable phase information is available, it is worth trying to extract it and use it with well-posed coherent imaging methods to obtain images with better resolution.

This paper takes the latter approach and presents a first attempt at enhancing the SNR of the array data by suppressing medium reverberations. It introduces filters, or annihila-

*Published electronically November 8, 2012. This paper originally appeared in *Multiscale Modeling & Simulation*, Volume 7, Number 3, 2009, pages 1267–1301.
http://www.siam.org/journals/sirev/54-4/88097.html

†Department of Computational and Applied Mathematics, Rice University, MS 134, Houston, TX 77005-1892 (borcea@caam.rice.edu). The work of this author was partially supported by AFSOR grant FA9550-12-1-0117, ONR grants N00014-12-1-0256, N00014-09-1-0290, and N00014-05-1-0699, and NSF grants DMS-0907746, DMS-0934594, and DMS-0604008.

‡Shell Oil Bellaire Technology Center, Houston, TX 77025 (F.Gonzalez-Del-Cueto@shell.com). The Ph.D. studies of this author were supported by ONR grant N00014-05-1-0699 and by NSF grants DMS-0604008, DMS-0305056, and DMS-0354658.

§Department of Mathematics, Stanford University, Stanford, CA 94305 (papanico@math.stanford.edu). The work of this author was partially supported by U.S. Army grant W911NF-07-2-0027-1 and by AFOSR grant FA9550-11-1-0266.

¶Department of Applied Mathematics, University of Crete and IACM/FORTH, GR-71409 Heraklion, Greece (tsogka@tem.uoc.gr). The work of this author was partially supported by European FP7 Marie Curie International Reintegration grant MIRG-CT-2007-203438 and the European Research Council under the European Union's Seventh Framework Programme (FP7/2007-2013)/ERC grant agreement 239959.

tors of layer backscatter, that are designed to remove primary echoes from strong, isolated layers in a medium with additional random layering at small, subwavelength scales. These strong layers are called deterministic because they can be imaged from the data. However, our goal is not to image the layers, but to suppress them and thus enhance the echoes from compact scatterers buried deep in the medium. Surprisingly, the layer annihilators work better than intended, in the sense that they suppress not only the echoes from the deterministic layers, but also multiply scattered ones in the randomly layered structure.

Following the layer annihilators presented here, other filters of general, nonlayered heavy clutter have been developed. We review these more recent developments and the challenges of imaging in heavy clutter in the introduction in order to place the research presented here in context. We then present in detail the layer annihilators and show with analysis and numerical simulations how they work.

Key words. broadband array imaging, random media, migration, coherent interferometry, velocity estimation

AMS subject classifications. 35R30, 60G35, 86A22

DOI. 10.1137/120880975

1. Introduction.

Sensor array imaging is an important technology in many applications such as ultrasonic nondestructive testing, seismic exploration, and ground or foliage penetrating radar. The arrays use one or more sources to probe a medium with signals that are typically short pulses, and then they record the reflected waves. Depending on the application, the waves may be acoustic, elastic, or electromagnetic. We consider here scalar, pressure waves, modeled by the acoustic wave equation. This simplifies the analysis while neglecting shear waves and mode conversion of elastic waves in solids, and polarization effects for electromagnetic waves.

The array data are the recordings of the pressure field $p(t, \vec{\mathbf{x}}_r, \vec{\mathbf{x}}_s)$, with $\vec{\mathbf{x}}_s$ and $\vec{\mathbf{x}}_r$ denoting the locations of the sources and receivers. We call the recordings time traces to emphasize their dependence on the time t that takes values in some recording window. In principle, the location of the sources and receivers may be in different sets. We assume here that they are collocated at N points in a set $\mathcal{A}$, the array. The array data are gathered with $N_s \leq N$ sources that sequentially probe the medium. All the N sensors in the array record the responses, the echoes. We may have the entire response matrix

$$\mathbb{P}(t) = \{p(t, \vec{\mathbf{x}}_r, \vec{\mathbf{x}}_s)\}_{r,s=1,\ldots,N}$$

when $N_s = N$, or just a column of it, in the case of a single source excitation. The imaging problem is to determine the reflectivity ν of the coherent scatterers in the medium. We often image just the support of the reflectivity, which is located around abrupt changes of the wave speed such as jump discontinuities that produce reflected waves measured at the array.

Imaging in smooth or homogeneous media, such as air, is simpler, because the waves are scattered only by the coherent scatterers that we wish to locate. It can be done efficiently with Kirchhoff migration and its variants used in radar [36, 44], seismic imaging [19, 41, 20], etc. These methods form an image in a search domain $\mathcal{D}$ by superposing the data traces $p(t, \vec{\mathbf{x}}_r, \vec{\mathbf{x}}_s)$ migrated to imaging points $\vec{\mathbf{y}}^s \in \mathcal{D}$. The term migration refers to the synchronization of the traces at time $t = \tau(\vec{\mathbf{x}}_r, \vec{\mathbf{y}}^s, \vec{\mathbf{x}}_s)$, the travel time from the source at $\vec{\mathbf{x}}_s$ to $\vec{\mathbf{y}}^s$ and then back to the array at receiver $\vec{\mathbf{x}}_r$.

The Kirchhoff migration function is given by

$$\mathcal{J}^{\mathrm{KM}}(\vec{\mathbf{y}}^s) = \sum_{\vec{\mathbf{x}}_s, \vec{\mathbf{x}}_r \in \mathcal{A}} p\big(\tau(\vec{\mathbf{x}}_r, \vec{\mathbf{y}}^s, \vec{\mathbf{x}}_s), \vec{\mathbf{x}}_r, \vec{\mathbf{x}}_s\big). \tag{1.1}$$

It is a simplification of the solution of the least squares optimization problem that estimates the unknown reflectivity ν in the medium by minimizing the misfit between the array data and its mathematical model linearized in the reflectivity [20]. More explicitly, (1.1) is the high frequency approximation of the L^2 adjoint $\mathcal{M}^\star$ of the forward map $\mathcal{M}$ applied to the data d. The forward map takes the reflectivity ν to the data space. The adjoint takes the data and backpropagates it to the imaging points by running the wave equation in reverse. Kirchhoff migration assumes that the medium is known and smooth, and it uses geometrical optics to approximate the backpropagation, up to an amplitude factor that is nearly constant, by evaluating the data at the travel times [20, 19].

The solution of the linear least squares formulation of the inverse problem satisfies the normal equations

$$\mathcal{M}^\star \mathcal{M} \nu = \mathcal{M}^\star d, \tag{1.2}$$

with $\mathcal{M}^\star\mathcal{M}$ the normal operator (Hessian). This is also called the time reversal operator, because, mathematically, it takes the data, time reverses it, and then backpropagates it to the imaging points. It turns out that $\mathcal{M}^\star\mathcal{M}$ focuses at the reflectivity, at least for large enough arrays and bandwidths, as shown in [17, 18, 67] in the case of smooth media. The relevance of these results to imaging is that the support of the unknown coherent scatterers can be estimated from the right-hand side of (1.2), the operator $\mathcal{M}^\star$ acting on the data, which is what (1.1) approximates in smooth media.

Recent studies, mostly applied to exploration geophysics, use full wave simulators instead of approximations with travel times, and they improve images by inverting the normal operator [54, 45, 58] in the generalized sense. Alternatively, images can be improved with image enhancement filters [29, 24] or by using regularization techniques based on prior information, such as sparsity of the scattering scenes [46, 13, 40]. All such results are dependent on the medium being smooth and known. If the medium is not known, but is smooth, it can be estimated with a complementary process called velocity estimation. Velocity estimation can be done separately, using tomographic methods [66, 16], or jointly with imaging [39].

Imaging is more complicated in heterogeneous media, with numerous inhomogeneities that cause significant cumulative scattering. The inhomogeneities arise at small, typically subwavelength scales. They cannot be known in advance and they cannot be estimated from the array data. We can only estimate the smooth part of the wave speed, called the background speed, which is what determines the travel time of the coherent part of the signals. The small scale details of the medium cannot be determined, they may not even be interesting in applications, but they cause scattering. For example, in nondestructive evaluation of aging concrete structures, the goal is to find coherent scatterers (defects) such as voids or cracks. These are strong scatterers when compared with any single inhomogeneity (pebble) in the concrete, but there are many inhomogeneities, and their scattering effects add up. The time traces measured at the array are noisy, with waves scattered back by the medium arriving long before and after the primary echoes from the defects. The primary echoes are the parts of the signals that are transmitted through the medium, scatter at the defects, and then are transmitted back to the array. They are the coherent part of

the data that we need for imaging, because we know how to relate their arrival times to locations of scatterers in the medium. Multiple scattering by the inhomogeneities gradually transfers the energy of the coherent signals to the incoherent echoes, the medium backscatter, which impedes imaging.

The numerous inhomogeneities in the medium are called clutter. Mathematically, they represent small scale fluctuations of the wave speed. Because the fluctuations are unknown, we model them with random processes and speak of wave propagation and imaging in random media. The "noise" in the measurements is the wave field backscattered by one realization of the random medium. It is very different than the additive, identically distributed, and uncorrelated noise commonly assumed in imaging. The clutter backscatter is not additive, it has complicated statistics, with correlations over sensor offsets and frequencies, and it is difficult to mitigate. For example, it follows from the law of large numbers that additive, uncorrelated noise can be removed by the sum over the sensors in (1.1) if N is large. Clutter backscatter has persistent correlations and it is not removed in (1.1). The resulting images are noisy (speckled) and difficult, or impossible, to interpret.

To explain in more detail the failure of Kirchhoff migration and related approaches in clutter, let us go back to the normal equations (1.2). The normal (time reversal) operator $\mathcal{M}^\star\mathcal{M}$ still focuses at the reflectivity. In fact, the focusing is better in clutter, meaning that it can occur even for small arrays, as described in the time reversal studies [47, 22, 60]. Thus, $\mathcal{M}^\star d$ would give a good estimate of the unknown reflectivity, if we could compute it. But $\mathcal{M}^\star$ is unknown, because the medium is unknown. Traditional methods like Kirchhoff migration ignore the unknown inhomogeneities and replace $\mathcal{M}^\star$ with a surrogate $\mathcal{M}_o^\star$. The surrogate backpropagates the data in a fictitious smooth medium. For example, this could be the medium with the known or estimated background speed, the mean of the rapidly fluctuating wave speed in clutter. Unfortunately, $\mathcal{M}_o^\star d$ is not a good approximation of the backpropagation in the real medium, and imaging fails.

An efficient way to mitigate clutter backscatter is to image with local cross-correlations of the time traces, instead of the traces themselves, as is done in the coherent interferometric (CINT) approach introduced and analyzed in [31, 30, 33, 26]. CINT imaging can be viewed as a statistically smoothed migration method. The smoothing is done by cross-correlating the traces over carefully chosen sensor offset and time windows, and then summing the results, synchronized with travel times relative to the imaging points. The choice of the windows plays a key role in the quality of CINT images, that is, their focusing and robustness. The optimal window sizes are given by two intrinsic scales that capture the statistics of the clutter backscatter: The decoherence frequency Ω_d and the decoherence length X_d, which varies with frequency. Typically, Ω_d is smaller than the bandwidth of the signals, and X_d is smaller than the array aperture. The decoherence frequency and length are defined as the frequency and sensor offsets over which clutter backscatter decorrelates. They depend on the statistics of the clutter, the distance of propagation, and the frequency. Expressions for Ω_d and X_d have been derived analytically, using various random models of clutter [33], but CINT is a general imaging approach that is not tied to a model. It has an adaptive implementation that estimates Ω_d and X_d during the image formation, without any prior knowledge of the medium [30, 26]. The resolution and statistical stability analysis of CINT are given in [33, 26], and shows that the CINT imaging function involves the Wigner transform of the array data smoothed over its arguments. The smoothing is needed for statistical stability, but it blurs the image. The smaller the sensor offset windows and the longer the temporal ones, the more smoothing CINT

does, at the expense of resolution. The trade-off between smoothing for stability and resolution leads to a figure of merit of the images that CINT produces, which is optimized in adaptive CINT to get the optimal choice of the windows over which to cross-correlate the data traces [30, 26].

CINT by itself cannot deal with heavy clutter. If the waves travel deep in the medium the signal-to-noise ratio (SNR) is very low. The clutter backscatter (the "noise") dominates the measurements at the array and the coherent echoes (the "signals") are faint. Imaging at such low SNR can proceed in two ways. One way is to accept that there is no coherence left in the data and work with intensities of the measured field [12, 4, 28]. The coherent scatterers are represented by parameters in diffusion or radiative transport equations that model the intensity, and the problem becomes a parameter estimation [12, 4]. The difficulty is that the estimation is extremely ill-posed, meaning that only very low resolution results can be expected, unless there is very good prior information about the coherent scatterers. Thus, if there is residual coherence in the array data, as faint as it may be, it is worth trying to extract it and then process it with well-posed, coherent methods such as CINT that give better resolution. This leads to the second way of dealing with low SNR, which complements the imaging process with data preprocessing that filters clutter backscatter, thus enhancing the SNR. The question is how to do the filtering, with no prior information about the location of the coherent scatterers to be imaged.

This paper describes one of the first filtering approaches, called layer annihilation. It is designed for imaging compact coherent scatterers buried deep in layered media. For example, the coherent scatterers may be due to fractures, small scale faults, rough edges of salt bodies, or other "diffractors," as they are called in the geophysics literature, in an idealized layered earth. Layered media are of special interest here because they represent the worst case scenario in terms of strength of clutter backscatter. The concept of transport mean free path that quantifies net scattering in general clutter does not even apply to randomly layered media, because of wave localization [5, 50, 64]. Wave localization means that all of the incident energy is reflected back and does not reach beyond some depth [71, 5, 50].

The layered media in this paper have random fluctuations of the wave speed at a fine length scale ℓ that is small with respect to the central wavelength λ_o of the waves emitted by the source. There are also isolated strong scattering layers, for example, due to large jump discontinuities of the wave speed. These layers are coherent scatterers that produce strong primary echoes at the array, and thus can be imaged. However, we are not concerned with imaging the layers. We look instead at how to enhance the primary echoes from compact scatterers buried deep in the medium, with no knowledge of the layered structure.

The separation of the layer echoes from those due to small diffractors has been considered before in the geophysics literature [42, 48]. Examples are the so-called plane-wave destruction filters [42, 48, 49] designed to remove from the data a sequence of plane-like waves arriving from different directions. The layer annihilators discussed in this paper use ideas from semblance velocity estimation [39, 68]. They are based on the fact that the arrivals from the small scatterers and the arrivals from the layers have a different signature in the time and source-receiver offset space. The layer annihilation consists of two steps. The first step is a travel-time transformation of the data, between the time t and the range z, the depth in the layered medium. The purpose of the transformation is to remove the dependence of the primary layer echoes on the source and receiver offset so that we can suppress them in the second step, by taking, for example, derivatives in the offset. The arrival times of the primary echoes

from the compact scatterers have a different dependence on the offset, and this is why they are not removed.

We show with analysis and numerical simulations that layer annihilators are efficient image enhancement tools, provided that we know the smooth part of the wave speed. If this is not known, we indicate briefly how it can be estimated by coupling the imaging process with an optimization scheme. The objective function measures the quality of the image as it is being formed with migration of the filtered data with a trial background speed. The annihilation is effective when the speed is right, and this is why we can estimate it directly by working with the image.

The analysis presented here explains the annihilation of the echoes from the strong layers. But what is surprising is that the incoherent backscatter from random layering is annihilated as well. The theoretical analysis of this surprising result is in [27].

Following the layer annihilation filters presented here, other approaches have emerged that work in general clutter, not just layered ones [6, 7, 8, 3, 51, 2, 35]. The one-to-one correspondence between time and depth traveled by the waves exists only in layered media, so filtering cannot be based just on travel-time transformations. New approaches have emerged that combine results from random matrix theory [57, 9, 10] with statistical tools from extreme value theory [1] and computational harmonic analysis [56] to detect faint coherent echoes in heavy clutter backscatter, and to enhance the SNR.

The algorithm introduced in [35] uses the local cosine transform (LCT) to decompose the traces, the entries in the response matrix $\mathbb{P}(t)$, in orthonormal bases given by smooth time windows modulated by cosine functions. It detects the time windows that contain the faint coherent echoes using the singular value decomposition of the transformed response matrix, for all the frequencies in the bandwidth. The window search is on a binary tree, starting from the root, and the detection is based on anomalous behavior of the largest singular values as functions of frequency and the time window. Once a window is selected, it is refined by taking the search to the children of the window, and so on. The filtering of clutter backscatter consists of three steps: First, it zeroes the LCT coefficients in all the time windows but the selected one. Second, it projects the matrix of LCT coefficients in the selected window on the subspace of low rank matrices with the anomalous large singular values, which contain information about the coherent scatterers. Third, it undoes the LCT and gives the filtered data in the original time window used by the array for recording the traces. The analysis of the algorithm in [35] is carried out in [2] in randomly layered media, where the response matrix has a special Toeplitz structure. This allows a detailed spectral analysis of the LCT matrices, using the tools developed in [53, 55, 38], and puts the detection and filtering approach in [35] into a rigorous setting, at least for layered media.

The detection of weak coherent echoes using the first singular value of the response matrix is also studied in [6, 7, 8, 3, 51] for the case of heavy isotropic clutter and for strong additive noise. It requires the estimation of the probability distribution of the singular value, so as to set a statistical detection threshold. The results in [6, 7, 8] include a filter of clutter backscatter that has been tested experimentally. It uses the paraxial approximation model of the primary echoes in combination with subspace projections to enhance the SNR.

A completely different approach for mitigating heavy clutter uses an auxiliary array of receivers that is near the imaging region [52, 11, 63, 70]. Near means closer than a transport scattering mean free path, so that scattering effects between the auxiliary array and the imaging region are not strong. The primary array is far away, and the signals emitted by its sources pass through heavy clutter to reach the

auxiliary array and the coherent scatterers. The auxiliary array records very noisy signals, the sequence of arrivals of the waves scattered multiple times during their passage through clutter. Some of these arrivals involve reflections at the coherent scatterers in the imaging region. The analysis in [52] shows that the primary echoes from these scatterers can be extracted efficiently from cross-correlations of the noisy measurements at the auxiliary array. The cross-correlations compress the long signals caused by heavy clutter, at the origin of time; that is, they have a large peak at $t = 0$. However, they also peak at the travel time between the auxiliary sensors and the coherent scatterers. Thus, the heavy clutter can be removed by windowing the cross-correlations, and images can be formed using migration if there is no residual clutter effect and, otherwise, with CINT. The result is as if data were gathered by the auxiliary array which is near the imaging region [52, 11, 63, 70].

If the application permits the use of auxiliary arrays, then they should be used because they allow a simple removal of heavy clutter effects. But in many cases this is not possible, so data preprocessing with filters of clutter backscatter is the only choice for enhancing the SNR. This is where the results of this paper, which is specialized to layered media, and those that followed [6, 7, 8, 3, 51, 2, 35] that apply to general media, fit in.

A recent extension of the layer annihilator filters considered in this paper applies to synthetic aperture radar imaging with motion estimation [21]. It uses travel-time transformations to divide the data into subsets of echoes from stationary targets and moving targets with unknown velocity. The separated data sets are then processed, as shown, for example, in [25], to estimate target motion and to image.

2. Setup and Outline of the Paper. We consider the inverse problem of imaging scatterers of small support, buried deep in a medium with layered structure. The setup is illustrated in Figure 2.1. We probe the medium with a short pulse emitted from a source at $\vec{\mathbf{x}}_s$ and record the echoes at receivers placed at $\vec{\mathbf{x}}_r$ for $r = 1, \ldots, N$. Let

$$\mathcal{A} = \left\{ \vec{\mathbf{x}}_r = (\mathbf{x}_r, 0) \in \mathbb{R}^d, \quad \mathbf{x}_r \in \mathbb{R}^{d-1}, \quad r = 1, \ldots, N \right\}, \quad d \geq 2,$$

be the set of receiver locations, and consider a system of coordinates in dimension $d \geq 2$, with range (depth) z axis normal to the layers. The array is on the surface $z = 0$ in the set of diameter a, the array aperture.

The data are one column $\{p(t, \vec{\mathbf{x}}_r, \vec{\mathbf{x}}_s)\}_{r=1,\ldots,N}$ of the response matrix $\mathbb{P}(t)$, for the source at $\vec{\mathbf{x}}_s$. The layer annihilation does not need more than one source, unlike

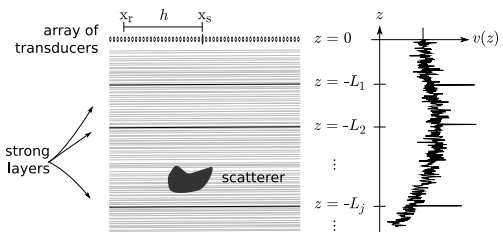

Fig. 2.1 *Schematic of the setup for imaging scatterers buried in a layered medium with wave speed $v(z)$. The array of transducers sits on top of the medium. The source and receiver locations are denoted by $\mathbf{x}_s$ and $\mathbf{x}_r$. The medium is finely layered, and it has some strong scattering interfaces at depths $-L_j$ for $j = 1, 2, \ldots$.*

the filters in [6, 7, 8, 3, 51, 2, 35] that work in general clutter but require the whole response matrix $\mathbb{P}(t)$. Because the source is fixed, we suppress it henceforth in the arguments of the pressure field.

The inverse problem is to use the data $\{p(t,\vec{\mathbf{x}}_r)\}_{r=1,\ldots,N}$ to locate the small scatterers in the layered medium, which may be known partially or not at all. By partial knowledge we mean that we may know the large scale features of the wave speed, but not its small scale fluctuations, which we model as random with length scale ℓ. The medium may also have strong scattering layers at depths $z = -L_j$ for $j = 1, 2, \ldots, M$. The depth of these layers is not known, although it can be estimated in principle from the data. We are not concerned with finding the layers. We look instead at how to suppress the layer echoes and therefore enhance those echoes from the small scatterers.

The random fluctuations are strong enough, of order one, and cause scattering that is visible in the traces as long tailed signals observed long before and long after the arrival of the echoes from the small scatterers. If we have separation of scales of the form

$$\ell \ll \lambda_o \ll L \tag{2.1}$$

and a broadband pulse, as assumed in this paper, then the data retains a coherent part. These are the echoes from the small scatterers and the strong layers at $z = -L_j$, for $j = 1, 2, \ldots, M$, and they are described by the O'Doherty–Anstey (ODA) theory [50, 5, 59, 43, 65]. ODA theory says that if we observe $p(t,\vec{\mathbf{x}}_r)$ in a time window of width similar to that of the probing pulse, centered at the travel time computed in the smooth part of the medium, for waves traveling between the array and the scatterers, we see a deterministic signal except for a small random arrival time shift. Such pulse stabilization is special to layered media and it is because of this that Kirchhoff migration can give useful results, in spite of the fine scale fluctuations. This has been noted in [32, 23] in the context of imaging sources buried in finely layered media.

However, Kirchhoff migration does not give useful results in the case of scatterers buried deep in layered media, due to low SNR. The echoes from the layers, the "noise," overwhelm the coherent arrivals, the signal, from the scatterers buried deep in the medium, and must be filtered from the data prior to imaging. We introduce such filters, called layer annihilators, and show that they can improve significantly the images, provided that we know the smooth part of the wave speed. If this is not known, we indicate briefly how it can be estimated by coupling the imaging process with an optimization scheme. The objective function measures the quality of the image as it is being formed by migrating the filtered data with a trial background speed. The annihilation is effective when the speed is right, and this is why we can estimate it directly by working with the image.

While all the theory in this paper assumes perfectly layered structures, we present numerical simulations in media with additional, isotropic fluctuations, generated by weak and small inhomogeneities of diameter comparable to λ_o. The cumulative effect of such inhomogeneities leads to significant loss of coherence of the echoes coming from the deep scatterers and consequently to the degradation of resolution and reliability of the Kirchhoff migration images, even after the layer annihilation process. The loss of coherence due to scattering by the inhomogeneities is dealt with efficiently by the coherent interferometric (CINT) imaging method.

The paper is organized as follows: We begin in section 3 with the mathematical model for the acoustic pressure recorded at the array. Then we introduce and analyze in section 4 the filters that we call layer annihilators. Imaging with these filters and

the coupling with velocity estimation are discussed in section 5. The numerical results are in section 6. We end with a summary and conclusions in section 7.

3. The Forward Model. The acoustic pressure $p(t,\vec{\mathbf{x}})$ and velocity $\vec{\mathbf{u}}(t,\vec{\mathbf{x}})$ satisfy the first order system of partial differential equations

$$\begin{aligned} \rho\frac{\partial\vec{\mathbf{u}}}{\partial t}(t,\vec{\mathbf{x}}) + \nabla p(t,\vec{\mathbf{x}}) &= \vec{\mathbf{F}}(t,\vec{\mathbf{x}}),\\ \frac{1}{V^2(\vec{\mathbf{x}})}\frac{\partial p}{\partial t}(t,\vec{\mathbf{x}}) + \rho\nabla\cdot\vec{\mathbf{u}}(t,\vec{\mathbf{x}}) &= 0, \quad \vec{\mathbf{x}}\in\mathbb{R}^d, \quad t>0, \end{aligned} \tag{3.1}$$

where ρ is the medium density and V is the wave speed. The source at $\vec{\mathbf{x}}_s$ is modeled by $\vec{\mathbf{F}}(t,\vec{\mathbf{x}})$ and acts at times $t\geq 0$. The medium is quiescent prior to the source excitation,

$$\vec{\mathbf{u}}(t,\vec{\mathbf{x}}) = \vec{\mathbf{0}}, \quad p(t,\vec{\mathbf{x}}) = 0, \quad t<0. \tag{3.2}$$

We suppose for simplicity that the density ρ is constant, but its variations can be included in the analysis as shown in [50, 5].

The wave speed $V(\vec{\mathbf{x}})$ is modeled as

$$\frac{1}{V^2(\vec{\mathbf{x}})} = \frac{1}{v^2(z)} + \nu(\vec{\mathbf{x}}), \tag{3.3}$$

where $\nu(\vec{\mathbf{x}})$ is the reflectivity of the scatterers that we wish to image. We let $\mathcal{S}$ be the compact support of $\nu(\vec{\mathbf{x}})$ and suppose that it lies at depth $z=-L$ and that its diameter is small with respect to the array aperture a. The background speed is denoted by $v(z)$ and has a smooth (or piecewise smooth) part $c(z)$ and a remaining rough part supported in the half space $z<0$,

$$\frac{1}{v^2(z)} = \begin{cases} \frac{1}{c^2(z)}\left[1+\sigma\mu\left(\frac{z}{\ell}\right)\right], & -L_j < z < -L_{j-1}, \quad j=1,\ldots,M,\\ \frac{1}{c_o^2}, & z\geq -L_0 = 0. \end{cases} \tag{3.4}$$

The rough part consists of fine layering at scale $\ell \ll \lambda_o$ and of strong scattering interfaces at depths $z=-L_j$ for $j=1,\ldots,M$. These interfaces could be the result of jump discontinuities of $c(z)$, or we could have sudden blips[1] in $v(z)$, due to large variations of $c(z)$ over a few isolated intervals of order λ_o, as illustrated in Figure 2.1. We refer the reader to section A.4 for the details of our mathematical model of the scattering interfaces.

The fine layering is modeled in (3.4) with a random process written in scaled form as $\sigma\mu(z/\ell)$. We let μ be a dimensionless, zero-mean random function of dimensionless argument, and we control the strength of the fluctuations with the parameter σ. We consider strong fluctuations, with $\sigma = O(1)$, and we impose the constraint

$$\sigma\,|\mu(z)| < 1 \quad \text{for all } z<0, \tag{3.5}$$

so that the right-hand side in (3.4) stays positive and bounded. See section 3.2 for details on the scaling and the random function μ.

[1] The waves sample most efficiently the variations of the wave speed at scales similar to the wavelength. This is why isolated changes (blips) of $c(z)$ over intervals of length $\sim\lambda_o$ produce strong echoes.

3.1. The Scattered Field. The pressure field recorded at the receivers consists of two parts: the direct arrival at time $|\vec{\mathbf{x}}_r - \vec{\mathbf{x}}_s|/c_o$ from the source at $\vec{\mathbf{x}}_s$, and the scattered field. The direct arrival carries no information about the medium, and it can be removed by tapering the data for $t \leq |\vec{\mathbf{x}}_r - \vec{\mathbf{x}}_s|/c_o$.

For time t less than the travel time $\tau^{\mathcal{S}}$ from the source to $\mathcal{S}$ and back, $p(t, \vec{\mathbf{x}}_r)$ consists of the echoes from the layers above the localized scatterers. These can be determined by solving the wave equation

$$\begin{aligned} \rho \frac{\partial \vec{\mathbf{u}}}{\partial t}(t, \vec{\mathbf{x}}) + \nabla p(t, \vec{\mathbf{x}}) &= \vec{\mathbf{F}}(t, \vec{\mathbf{x}}), \\ \frac{1}{v^2(z)} \frac{\partial p}{\partial t}(t, \vec{\mathbf{x}}) + \rho \nabla \cdot \vec{\mathbf{u}}(t, \vec{\mathbf{x}}) &= 0, \quad \vec{\mathbf{x}} \in \mathbb{R}^d, \quad 0 < t < \tau^{\mathcal{S}}, \end{aligned} \tag{3.6}$$

with initial conditions (3.2), and then removing the direct arrival. Here we used the causality of the wave equation to ignore the reflectivity $\nu(\vec{\mathbf{x}})$ for $t < \tau^{\mathcal{S}}$.

For $t > \tau^{\mathcal{S}}$ the scattered field contains the echoes $p^{\mathcal{S}}(t, \vec{\mathbf{x}}_r)$ from the reflectivity $\nu(\vec{\mathbf{x}})$. We model them with the Born approximation

$$p^{\mathcal{S}}(t, \vec{\mathbf{x}}_r) \approx - \int_{\mathcal{S}} d\vec{\mathbf{y}}\, \nu(\vec{\mathbf{y}})\, \frac{\partial^2 p^i(t, \vec{\mathbf{y}})}{\partial t^2} \star_t G(t, \vec{\mathbf{x}}_r, \vec{\mathbf{y}}), \tag{3.7}$$

where $\star_t$ denotes time convolution and G is the causal Green's function of the wave equation in the layered medium:

$$\begin{aligned} \frac{1}{v^2(z)} \frac{\partial^2 G(t, \vec{\mathbf{x}}, \vec{\mathbf{y}})}{\partial t^2} - \Delta G(t, \vec{\mathbf{x}}, \vec{\mathbf{y}}) &= \delta(\vec{\mathbf{x}} - \vec{\mathbf{y}})\delta(t), \\ G(t, \vec{\mathbf{x}}, \vec{\mathbf{y}}) &= 0 \quad \text{for } t < 0. \end{aligned} \tag{3.8}$$

In (3.8) we denote by $p^i(t, \vec{\mathbf{x}})$ the "incident" pressure field, i.e., the field in the layered medium without the reflectivity. This satisfies (3.6) for all times $t > 0$ or, equivalently, it satisfies

$$\begin{aligned} \frac{1}{v^2(z)} \frac{\partial^2 p^i(t, \vec{\mathbf{x}})}{\partial t^2} - \Delta p^i(t, \vec{\mathbf{x}}) &= -\nabla \cdot \vec{\mathbf{F}}(t, \vec{\mathbf{x}}), \quad t > 0, \\ p^i(t, \vec{\mathbf{x}}) &= 0 \quad \text{for } t < 0. \end{aligned} \tag{3.9}$$

Note the similarity of (3.8) and (3.9). They both have as a source term a distribution supported at a point (at $\vec{\mathbf{x}}_s$ in (3.9) and at $\vec{\mathbf{y}} \in \mathcal{S}$ in (3.8)). This observation and (3.7) allow us to reduce the calculation of the scattered field to solving a generic problem for the pressure in a purely layered medium and for a point source excitation. We study this generic problem in detail in Appendix A. The resulting mathematical model of the scattered pressure field recorded at the array is presented in section 3.3.

3.2. Scaling. Let us consider the following model for the source excitation:

$$\vec{\mathbf{F}}(t, \vec{\mathbf{x}}) = \delta(\vec{\mathbf{x}} - \vec{\mathbf{x}}_s) \begin{pmatrix} \mathbf{F}^\epsilon(t) \\ f^\epsilon(t) \end{pmatrix}, \tag{3.10}$$

where

$$f^\epsilon(t) = \epsilon^{\frac{d-1}{2}} f\left(\frac{t}{\epsilon}\right), \quad \mathbf{F}^\epsilon(t) = \epsilon^{\frac{d-1}{2}} \mathbf{F}\left(\frac{t}{\epsilon}\right), \tag{3.11}$$

and $\epsilon \ll 1$. Here f is the pulse shape emitted upwards and $\mathbf{F} \in \mathbb{R}^{d-1}$ is the pulse in the remaining $d-1$ cross-range directions. The small parameter ϵ in the arguments in (3.11) comes from scaling the width of the pulse by the much longer travel time $\tau^{\mathcal{S}}$ of the waves from the source to the scatterers in $\mathcal{S}$ and back. Since the problem is linear we can control the amplitude of the echoes with the amplitude of the source. We take the latter equal to $\epsilon^{\frac{d-1}{2}}$ to obtain $O(1)$ echoes at the array.

In the frequency domain we have

$$\hat{f}^{\epsilon}\left(\frac{\omega}{\epsilon}\right) = \int dt\, f^{\epsilon}(t) e^{i\frac{\omega}{\epsilon}t} = \epsilon^{\frac{d+1}{2}} \int \frac{dt}{\epsilon} f\left(\frac{t}{\epsilon}\right) e^{i\omega\frac{t}{\epsilon}} = \epsilon^{\frac{d+1}{2}} \hat{f}(\omega), \tag{3.12}$$

and similarly for $\hat{\mathbf{F}}^{\epsilon}\left(\frac{\omega}{\epsilon}\right)$. Thus, assuming pulses $\hat{f}(\omega)$ and $\hat{\mathbf{F}}(\omega)$ with support in an $O(1)$ interval centered at ω_o, we see that the scaling in (3.10) implies having $O(1/\epsilon)$ frequencies in the analysis. Equivalently, the wavelengths are $\sim \epsilon$ while $L = O(1)$.

The random process μ that models the fluctuations of $v(z)$ has mean zero, is statistically homogeneous, and lacks long range correlations:

$$\mathcal{C}(z) = E\left\{\mu(0)\mu(z)\right\} \to 0 \quad \text{as } |z| \to \infty, \tag{3.13}$$

where the decay is sufficiently fast for $\mathcal{C}(z)$ to be integrable over the real line. We assume further the normalization

$$\mathcal{C}(0) = 1, \quad \int_{-\infty}^{\infty} \mathcal{C}(z)dz = 1, \tag{3.14}$$

which implies

$$\int_{-\infty}^{\infty} E\left\{\mu(0)\mu\left(\frac{z}{\ell}\right)\right\} dz = \ell, \tag{3.15}$$

where ℓ is the correlation length of the speed fluctuations. The intensity of the fluctuations is

$$E\left\{\left[\sigma\mu\left(\frac{z}{\ell}\right)\right]^2\right\} = \sigma^2, \tag{3.16}$$

and we control it by adjusting the dimensionless parameter σ.

Following [50], we refer to the scaling in this paper as a *high frequency, white noise regime*,

$$\frac{L}{\lambda_o} \gg 1, \quad \frac{\lambda_o}{\ell} \gg 1, \quad \sigma = O(1), \tag{3.17}$$

which arises in applications of exploration seismology [71], where $\lambda_o \sim 100\text{m}$, $L = 5 - 15\text{km}$, and $\ell = 2 - 3\text{m}$. The regime (3.17) considers strong fluctuations ($\sigma \sim 1$), but, since $\lambda_o \gg \ell$, the waves do not interact strongly with the small scales and the fluctuations average out over distances of order λ_0. It takes long distances of propagation ($L \gg \lambda_o$) for the scattering to build up and become an important factor in the problem.

We realize the regime (3.17) by taking

$$\frac{\ell}{\lambda_o} \sim \frac{\lambda_o}{L} \sim \epsilon \ll 1, \quad \sigma = 1, \quad L_j - L_{j-1} = O(1), \quad j = 1, 2 \ldots, \tag{3.18}$$

and we remark that we call it *high frequency* because the wavelengths are small in comparison with the large scale variations of the medium (i.e., L and $L_j - L_{j-1}$ for $j = 1, 2, \ldots$). It is, however, a low frequency regime with respect to the small scale ($\lambda_o \gg \ell$), and the effect of the random fluctuations takes the canonical form of *white noise* in the limit $\epsilon \to 0$, independent of the details of the random model μ [50, 5].

Let us note that there are other interesting scaling regimes where scattering is significant and the analysis can be carried out [50]. For example, the theory extends almost identically to the *weakly heterogeneous* regime

$$\ell \sim \lambda_o \ll L = O(1), \quad \sigma \ll 1, \tag{3.19}$$

except for some subtle differences [50]. In the scaling (3.19), the waves sample more efficiently the small scales, since $\ell \sim \lambda_o$, and the asymptotic theory results depend on the specific autocorrelation function of the random fluctuations [50]. In our regime the waves cannot see the small scales in detail, because $\lambda_o \gg \ell$, and this is why the theory is not sensitive to the precise structure of the random function μ.

The remaining scales are the array aperture a and the diameter b of the support $\mathcal{S}$ of the reflectivity ν. We assume that a is much larger than λ_o and independent of ϵ,

$$\lambda_o \ll a \leq L, \tag{3.20}$$

and that b satisfies

$$\lambda_o \leq b \ll a. \tag{3.21}$$

While b can be much larger than λ_o, it should be much smaller than a so that the layer annihilator filters can make a robust differentiation between the layer echoes and the coherent arrivals from $\mathcal{S}$.

3.3. The Multiple Scattering Series. We show in Appendix A that the pressure field at the surface $z = 0$ has the following multiple scattering series representation:

$$D(t, \mathbf{h}) := p(t, \vec{\mathbf{x}}) = \sum_{\mathcal{P}} \Phi_{\mathcal{P}} \left[\frac{t - \tau_{\mathcal{P}}(\mathbf{h})}{\epsilon} - \delta\tau_{\mathcal{P}}(\mathbf{h}), \mathbf{h} \right] + \mathcal{N}(t, \mathbf{h}). \tag{3.22}$$

Here $\vec{\mathbf{x}} = (\mathbf{x}, 0) \in \mathcal{A}$ is an arbitrary receiver location and

$$\mathbf{h} = \mathbf{x} - \mathbf{x}_s \tag{3.23}$$

is the source-receiver offset. Since the source is fixed at $\vec{\mathbf{x}}_s$, we can parametrize the data by the offset $\mathbf{h}$ and denote it from now on by $D(t, \mathbf{h})$. We also assume for convenience in the analysis that the separation between the receivers is small enough to allow us to view the array as a continuum aperture. This means that $\mathbf{h}$ varies continuously in a compact set of diameter a, the array aperture.

Data $D(t, \mathbf{h})$ consists of an incoherent part $\mathcal{N}$ and a coherent part. The incoherent part is due to scattering by the random medium between the strong layers. The coherent part is written in (3.22) as a sum of arrivals of pulses of shape $\Phi_{\mathcal{P}}$ along the multiple scattering paths $\mathcal{P}$. These paths are transmitted through the random medium, and they involve scattering in $\mathcal{S}$ and/or at the layers $z = -L_j$ for $j = 1, \ldots, M$. See Figure 3.1 for an illustration of coherent paths $\mathcal{P}$. It follows from Appendix A that these paths obey Snell's laws [37] at the scattering interfaces and

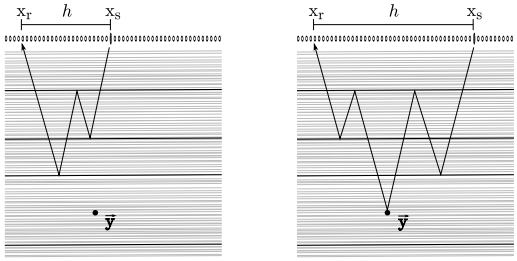

Fig. 3.1 *Examples of coherent paths from the source at $\vec{\mathbf{x}}_s$ to a receiver at $\vec{\mathbf{x}}_r$. Left: Path between the layers without "seeing" the scatterer at $\vec{\mathbf{y}}$. Right: Path through the scatterer at $\vec{\mathbf{y}}$.*

they pass through the random slabs $-L_j < z < -L_{j-1}$, for $j = 1, \ldots, M$, according to Fermat's principle [37].

The transmission of the waves through the random slabs is described in the asymptotic limit $\epsilon \to 0$ by the ODA theory. This says that as the pressure waves $p(t, \vec{\mathbf{x}})$ propagate through the random medium, they maintain a coherent front $p^{\mathrm{ODA}}(t, \vec{\mathbf{x}})$ that is similar to the field in the smooth medium, except for two facts: (1) The travel time has a small random shift $\epsilon\delta\tau$. (2) The pulse shape is broadened due to the convolution with a Gaussian kernel. This kernel accounts for the diffusion of energy from the coherent part of p to the incoherent part, and it is due to the multiple scattering in the finely layered structure.

The theory (see Appendix A and [50, 5, 59, 43, 65]) says that the amplitude of the incoherent events $\mathcal{N}(t, \mathbf{h})$ is smaller than the amplitude of the coherent events, by a factor of $O(\epsilon^{1/2})$. The amplitude of the coherent events varies by path. The variations are due to geometrical spreading, the reflection and transmission coefficients at the scattering interfaces, and the ODA pulse broadening in the random medium. The amplitudes and the time shifts $\epsilon\delta\tau_{\mathcal{P}}(\mathbf{h})$ change slowly with the offset $\mathbf{h}$. The fast variation of $D(t, \mathbf{h})$ with the offset is due to the $O(1/\epsilon)$ argument of $\Phi_{\mathcal{P}}$ in (3.22). This is the key observation used in section 4 to design layer annihilators for enhancement of the coherent arrivals along paths $\mathcal{P}_{\vec{\mathbf{y}}}$ through points $\vec{\mathbf{y}}$ in the support $\mathcal{S}$ of the reflectivity that we wish to image. Such signal enhancement is crucial for successful imaging of scatterers buried deep in the layered structure, as illustrated next.

3.3.1. An Illustration. For the purpose of illustration, let us consider the following simplification of our problem: Suppose that the source at $\vec{\mathbf{x}}_s$ has directivity along the z axis (i.e., $\mathbf{F}^\epsilon = \mathbf{0}$ in (3.10)) and that the smooth background has constant speed $c(z) = c_o$. Then, let us observe the pressure field $p(t, \vec{\mathbf{x}})$ for times $t < 2L_1/c_o$, so that we can ignore the scattering interface at $z = -L_1$. If there were no random fluctuations, the pressure field would be

$$p_o(t, \vec{\mathbf{x}}) = -\frac{\partial}{\partial z}\left[\frac{f^\epsilon\left(t - \tau(\vec{\mathbf{x}}, \vec{\mathbf{x}}_s)\right)}{4\pi|\vec{\mathbf{x}} - \vec{\mathbf{x}}_s|}\right], \quad \vec{\mathbf{x}} = (\mathbf{x}, z) \in \mathbb{R}^3. \tag{3.24}$$

We would observe the emitted pulse f centered at travel time $\tau(\vec{\mathbf{x}}, \vec{\mathbf{x}}_s) = |\vec{\mathbf{x}} - \vec{\mathbf{x}}_s|/c_o$, and the amplitude change due to geometrical spreading. The ODA theory says that the transmitted field through the random medium is given by [50, 5, 59, 43, 65]

$$p^{\mathrm{ODA}}(t, \vec{\mathbf{x}}) \approx -\frac{\partial}{\partial z}\left[\frac{\left(f^\epsilon \star_t \mathcal{K}^{\mathrm{ODA}}\right)\left(t - \tau(\vec{\mathbf{x}}, \vec{\mathbf{x}}_s) - \epsilon\delta\tau(\vec{\mathbf{x}}, \vec{\mathbf{x}}_s)\right)}{4\pi|\vec{\mathbf{x}} - \vec{\mathbf{x}}_s|}\right]. \tag{3.25}$$

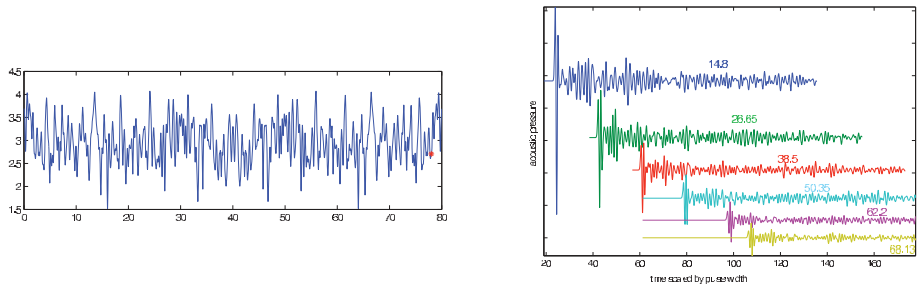

Fig. 3.2 *Left: The wave speed $v(z)$ as a function of depth measured in central wavelengths. Right: The transmitted pressure field for different depths traveled in the random medium. The depth for each trace is measured in central wavelengths.*

We have pulse spreading due to the convolution of f^ϵ with the Gaussian kernel

$$\mathcal{K}^{\rm ODA}(t) = \frac{\sin\theta(\vec{\mathbf{x}})}{\sqrt{2\pi}t_{\rm ps}(z)} e^{-\frac{t^2\sin^2\theta(\vec{\mathbf{x}})}{2t_{\rm ps}^2(z)}}, \quad \sin\theta(\vec{\mathbf{x}}) = \frac{|z|}{|\vec{\mathbf{x}}-\vec{\mathbf{x}}_s|}, \tag{3.26}$$

and a random arrival time shift $\epsilon\delta\tau(\vec{\mathbf{x}},\vec{\mathbf{x}}_s)$. The spread is proportional to $t_{\rm ps}(z)$, a parameter with units of time that depends on the correlation function $\mathcal{C}(z)$ of the random medium and the depth z, and it is more pronounced for waves propagating at shallow angles $\theta(\vec{\mathbf{x}})$. The time shift $\delta\tau(\vec{\mathbf{x}},\vec{\mathbf{x}}_s)$ is given by

$$\delta\tau(\vec{\mathbf{x}},\vec{\mathbf{x}}_s) = \frac{t_{\rm ps}(z)}{\sin\theta(\vec{\mathbf{x}})}\frac{W(z)}{\sqrt{|z|}}, \tag{3.27}$$

in terms of the standard Brownian motion $W(z)$.

We show in Figure 3.2 the pressure field computed with numerical simulations in two dimensions. The numerical method and setup are described in section 6. We plot on the left the wave speed $v(z)$, which fluctuates at length scale $\ell = 0.1\lambda_o$ around the constant value $c_o = 3$km/s. On the right we show the transmitted pressure field to five different depths ranging from $14\lambda_o$ to $68\lambda_o$. The ODA formula (3.25) describes the coherent fronts but not the incoherent long tail or coda. The theory [50, 5, 59, 43, 65] says that the amplitude of the coda is smaller than the coherent front, by a factor of $O(\epsilon^{1/2})$. This is what we see approximately in Figure 3.2.

In imaging we do not observe the transmitted field plotted in Figure 3.2. The array of sensors sits at the top surface $z = 0$ and records the scattered pressure field. We show in Figure 3.3 the pressure at the array for the numerical simulation setup shown on the left of the figure (see section 6 for details). We have a cluster of three small scatterers buried deep in the layered structure, below some strong scattering interfaces. Note the two strong coherent arrivals of the waves scattered by the top interfaces. Ahead of these arrivals we observe the incoherent signal due to the scattering by the fine layers. This signal is weak, consistent with the theory which says that the incoherent amplitudes are smaller than the coherent ones by a factor of $O(\epsilon^{1/2})$. The echoes from the small scatterers buried deep in the medium are also weak, and they cannot be distinguished in Figure 3.3 from the echoes due to the layers. This is a serious issue. It says that unless we can filter the data to enhance the signal from the small scatterers with respect to the echoes from the layers, we cannot image the scatterers.

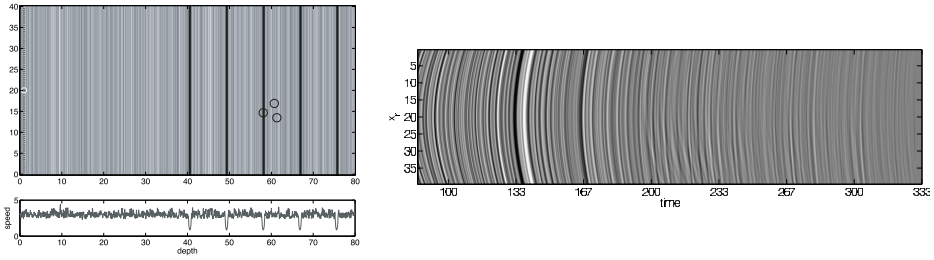

Fig. 3.3 *Left: Simulation setup with a cluster of three scatterers buried in a layered structure with speed $v(z)$ plotted below the computational domain. Right: Data traces plotted as a function of time (abscissa) and source-receiver offset (ordinate). The distances are scaled by the central wavelength and the time is scaled by the pulse width, which is* 0.02s *in our simulations.*

4. Layer Annihilators. In this section we define and analyze data filtering operators called layer annihilators. The performance of these filters depends on the background speed $c(z)$ and on whether we know it. The easiest and most favorable case is that of a homogeneous background, considered in section 4.1. The general case is discussed in section 4.2.

4.1. Homogeneous Background. We begin by analyzing the arrival times of the coherent events in the series (3.22). The paths $\mathcal{P}$ that do not involve scattering in $\mathcal{S}$ can be classified as the "primary paths" $\mathcal{P}_j$ that involve a single scattering at an interface $z = -L_j$, for $j = 1, \ldots, M$, and the "multiple paths" that are scattered more than once by the interfaces. See Figure 4.1 for an illustration of these paths. The red line indicates a primary path, the blue line indicates a multiple path, and the green line indicates a path $\mathcal{P}_{\vec{\mathbf{y}}}$ scattered at a point $\vec{\mathbf{y}}$ in $\mathcal{S}$.

The travel time along paths $\mathcal{P}_j$ is (see section A.6)

$$\tau_{\mathcal{P}_j}(\mathbf{h}) = T(h, L_j) = \frac{\sqrt{h^2 + 4L_j^2}}{c_o}, \tag{4.1}$$

where we let $h = |\mathbf{h}|$. Consider next a multiple path $\mathcal{P}$. Each reflection in $\mathcal{P}$ satisfies Snell's law, as shown in Appendix A. It also follows from Appendix A that the transmission through the random medium and through the interfaces does not bend the coherent paths, because the background speed is constant. This implies, after a straightforward geometrical argument, that any multiple path $\mathcal{P}$ has the same length as a primary path reflected at a ghost layer $z = -L_{\text{ghost}}$,

$$\tau_{\mathcal{P}}(\mathbf{h}) = T(h, L_{\text{ghost}}). \tag{4.2}$$

See Figure 4.1 for an illustration, where the multiple path shown in blue is mapped to the primary path (blue dotted line) reflected at the ghost layer shown with the black dotted line.

The arrival times along paths $\mathcal{P}_{\vec{\mathbf{y}}}$, for $\vec{\mathbf{y}} = (\mathbf{y}, -L) \in \mathcal{S}$, have a different dependence on the offset. Take, for example, the path that scatters at $\vec{\mathbf{y}}$ but involves no reflection by the layered structure (like the green path in Figure 4.1). The arrival time along $\mathcal{P}_{\vec{\mathbf{y}}}$ is

$$\tau_{\mathcal{P}_{\vec{\mathbf{y}}}}(\mathbf{h}) = \frac{1}{c_o}\left(\sqrt{|\mathbf{x}_s - \mathbf{y}|^2 + L^2} + \sqrt{|\mathbf{x}_s + \mathbf{h} - \mathbf{y}|^2 + L^2}\right) = T\left(h, \eta(\mathbf{h})\right), \tag{4.3}$$

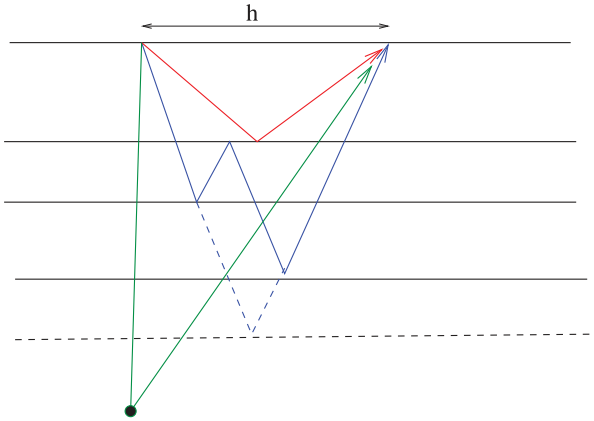

Fig. 4.1 *Illustration of a primary path (red), a multiple path (blue), and a path through a point scatterer (green). At background speed c_o the multiple path maps exactly to a primary reflection at a ghost interface drawn with the dotted line.*

and using the monotonicity in the second argument of (4.1), we can always equate it to the arrival time $T(h, \eta(\mathbf{h}))$ of a primary path from depth $-\eta(\mathbf{h})$. However, unlike $L_{\rm ghost}$ in (4.2), this depth depends on the offset

(4.4)
$$\eta(\mathbf{h}) = \left\{ \frac{L^2}{2} + \frac{(\mathbf{x}_s - \mathbf{y}) \cdot (\mathbf{x}_s + \mathbf{h} - \mathbf{y})}{2} + \frac{1}{2} \left[\left(|\mathbf{x}_s - \mathbf{y}|^2 + L^2 \right) \left(|\mathbf{x}_s + \mathbf{h} - \mathbf{y}|^2 + L^2 \right) \right]^{\frac{1}{2}} \right\}^{\frac{1}{2}}.$$

It is only in the case of $\vec{\mathbf{y}}$ below the midpoint between the source and receiver (i.e., $\mathbf{y} = \mathbf{x}_s + \mathbf{h}/2$) that $\eta(\mathbf{h})$ is independent of $\mathbf{h}$. Considering that the source is fixed in our data acquisition setup, this is a special situation that can arise for at most one offset $\mathbf{h}$.

The layer annihilators are data filtering operators intended to suppress all coherent arrivals at times $T(h, z)$ for arbitrary depths $z < 0$. We study theoretically and numerically two such annihilators. Since the background speed c_o may not be known, we define them at a trial speed $\tilde{c}_o$. We then show in section 5 how to use the annihilators for imaging and velocity estimation.

DEFINITION 4.1. *Consider a trial $\tilde{c}_o$ of the true background speed and define function*

$$T_{\tilde{c}_o}(h, z) = \frac{\sqrt{h^2 + 4z^2}}{\tilde{c}_o} \tag{4.5}$$

and its inverse

$$\zeta_{\tilde{c}_o}(h, t) = -\frac{\sqrt{\tilde{c}_o^2 t^2 - h^2}}{2}, \tag{4.6}$$

where

$$T_{\tilde{c}_o}\left(h, \zeta_{\tilde{c}_o}(h, t)\right) = t, \quad \zeta_{\tilde{c}_o}\left(h, T_{\tilde{c}_o}(h, z)\right) = z. \tag{4.7}$$

We propose as a layer annihilator the data filtering operator $\mathbb{Q}_{\tilde{c}_o}$:

$$\left[\mathbb{Q}_{\tilde{c}_o} D\right](t, \mathbf{h}) = \left[\frac{d}{dh} D\left(T_{\tilde{c}_o}(h, z), \mathbf{h}\right) \right]_{z = \zeta_{\tilde{c}_o}(h,t)}. \tag{4.8}$$

This definition involves three steps: (1) The mapping of the data from the time and offset space (t,h) to the time and depth space (t,z), via function $T_{\tilde{c}_o}(h,z)$. This is called normal move-out in the geophysics literature [42, 19]. (2) Annihilation via the derivative with respect to h. The derivative is expected to be small if we indeed have echoes at times $T(h,z)$, for some z, because the normal move-out eliminates by subtraction the strong variation of $\Phi_{\mathcal{P}}$ in h (see (3.22)). (3) The return to the (t,h) space with the inverse function $\zeta_{\tilde{c}_o}$.

We have the following result.

LEMMA 4.2. *The operator $\mathbb{Q}_{\tilde{c}_o}$ is a layer annihilator, in the sense that it suppresses the echoes from the layered structure if $\tilde{c}_o = c_o + O(\epsilon)$. The operator does not suppress the echoes from the compactly supported reflectivity for any trial speed.*

Proof. The result follows easily from the discussion at the beginning of this section. The goal of the annihilator is to suppress the coherent paths that involve scattering by the layered structure. According to (4.1) and (4.2), the arrival time along these paths is of the form $T_{c_o}(h, L_{\mathcal{P}})$ for some layer at a depth $-L_{\mathcal{P}}$:

$$\Phi_{\mathcal{P}}\left[\frac{t-\tau_{\mathcal{P}}(\mathbf{h})}{\epsilon} - \delta\tau_{\mathcal{P}}(\mathbf{h}), \mathbf{h}\right] = \Phi_{\mathcal{P}}\left[\frac{t-T_{c_o}(h,L_{\mathcal{P}})}{\epsilon} - \delta\tau_{\mathcal{P}}(\mathbf{h}), \mathbf{h}\right].$$

After normal move-out, we get

$$\Phi_{\mathcal{P}}\left[\frac{T_{\tilde{c}_o}(h,z) - T_{c_o}(h,L_{\mathcal{P}})}{\epsilon} - \delta\tau_{\mathcal{P}}(\mathbf{h}), \mathbf{h}\right],$$

with z to be mapped later to time t, using $\zeta_{\tilde{c}_o}(h,t)$. Now take the derivative with respect to $h = |\mathbf{h}|$ and let $\mathbf{e_h}$ be the unit vector in the direction of $\mathbf{h}$. We have

(4.9)
$$\left\{\frac{1}{\epsilon}\frac{d}{dh}\left[T_{\tilde{c}_o}(h,z) - T_{c_o}(h,L_{\mathcal{P}})\right] - \mathbf{e_h}\cdot\nabla\delta\tau_{\mathcal{P}}(\mathbf{h})\right\}\frac{\partial}{\partial t}\Phi_{\mathcal{P}}\left[\frac{T_{\tilde{c}_o}(h,z)-\tau_{\mathcal{P}}(\mathbf{h})}{\epsilon} - \delta\tau_{\mathcal{P}}(\mathbf{h}), \mathbf{h}\right]$$
$$+ \mathbf{e_h}\cdot\nabla_{\mathbf{h}}\Phi_{\mathcal{P}}\left[\frac{T_{\tilde{c}_o}(h,z)-\tau_{\mathcal{P}}(\mathbf{h})}{\epsilon} - \delta\tau_{\mathcal{P}}(\mathbf{h}), \mathbf{h}\right],$$

where we denote by $\frac{\partial}{\partial t}\Phi_{\mathcal{P}}$ the derivative of $\Phi_{\mathcal{P}}$ with respect to the first argument and by $\nabla_{\mathbf{h}}\Phi_{\mathcal{P}}$ the gradient with respect to the second argument. Recall from section 3.3 and section A.6 that $\Phi_{\mathcal{P}}(\cdot,\mathbf{h})$ and $\delta\tau_{\mathcal{P}}(\mathbf{h})$ vary slowly in $\mathbf{h}$. The leading term in (4.9) is

$$\frac{1}{\epsilon}\frac{d}{dh}\left[T_{\tilde{c}_o}(h,z) - T_{c_o}(h,L_{\mathcal{P}})\right]\frac{\partial}{\partial t}\Phi_{\mathcal{P}}\left[\frac{T_{\tilde{c}_o}(h,z)-\tau_{\mathcal{P}}(\mathbf{h})}{\epsilon} - \delta\tau_{\mathcal{P}}(\mathbf{h}), \mathbf{h}\right]$$
$$= \frac{1}{\epsilon}\left[\frac{h}{\tilde{c}_o^2 T_{\tilde{c}_o}(h,z)} - \frac{h}{c_o^2\tau_{\mathcal{P}}(\mathbf{h})}\right]\frac{\partial}{\partial t}\Phi_{\mathcal{P}}\left[\frac{T_{\tilde{c}_o}(h,z)-\tau_{\mathcal{P}}(\mathbf{h})}{\epsilon} - \delta\tau_{\mathcal{P}}(\mathbf{h}), \mathbf{h}\right],$$

and after mapping $z = \zeta_{\tilde{c}_o}(h,t)$, it becomes

$$\frac{1}{\epsilon}\left[\frac{h}{\tilde{c}_o^2 t} - \frac{h}{c_o^2\tau_{\mathcal{P}}(\mathbf{h})}\right]\frac{\partial}{\partial t}\Phi_{\mathcal{P}}\left[\frac{t-\tau_{\mathcal{P}}(\mathbf{h})}{\epsilon} - \delta\tau_{\mathcal{P}}(\mathbf{h}), \mathbf{h}\right].$$

Since $\Phi_{\mathcal{P}}$ has $O(1)$ support, the leading order term can be observed at times $t = \tau_{\mathcal{P}}(\mathbf{h}) + O(\epsilon)$,

$$\left(\frac{1/\tilde{c}_o^2 - 1/c_0^2}{\epsilon}\right)\frac{h}{\tau_{\mathcal{P}}(\mathbf{h})}\frac{\partial}{\partial t}\Phi_{\mathcal{P}}\left[\frac{t-\tau_{\mathcal{P}}(\mathbf{h})}{\epsilon} - \delta\tau_{\mathcal{P}}(\mathbf{h}), \mathbf{h}\right] + O(1),$$

and then only if $|\tilde{c}_o - c_o| > O(\epsilon)$.

Let us consider next the coherent arrivals along paths $\mathcal{P}_{\vec{\mathbf{y}}}$ scattered at points $\vec{\mathbf{y}} \in \mathcal{S}$. We focus our attention on the "stronger" paths[2] that involve no scattering in the layered structure. Using a calculation similar to the above, we get

$$\frac{d}{dh}\Phi_{\mathcal{P}_{\vec{\mathbf{y}}}}\left[\frac{T_{\tilde{c}_o}(h,z)-\tau_{\mathcal{P}_{\vec{\mathbf{y}}}}(\mathbf{h})}{\epsilon}-\delta\tau_{\mathcal{P}_{\vec{\mathbf{y}}}}(\mathbf{h}),\mathbf{h}\right]\Bigg|_{z=\zeta_{\tilde{c}_o}(h,t)}$$
$$=\frac{1}{\epsilon}\left[\frac{h}{\tilde{c}_o^2 t}-\frac{h}{c_o^2\tau_{\mathcal{P}_{\vec{\mathbf{y}}}}(\mathbf{h})}\right]\frac{\partial}{\partial t}\Phi_{\mathcal{P}_{\vec{\mathbf{y}}}}\left[\frac{t-\tau_{\mathcal{P}_{\vec{\mathbf{y}}}}(\mathbf{h})}{\epsilon}-\delta\tau_{\mathcal{P}_{\vec{\mathbf{y}}}}(\mathbf{h}),\mathbf{h}\right]$$
$$+\frac{2}{\epsilon c_o^2\tau_{\mathcal{P}_{\vec{\mathbf{y}}}}(\mathbf{h})}\mathbf{e_h}\cdot\nabla\eta^2(\mathbf{h})\frac{\partial}{\partial t}\Phi_{\mathcal{P}_{\vec{\mathbf{y}}}}\left[\frac{t-\tau_{\mathcal{P}_{\vec{\mathbf{y}}}}(\mathbf{h})}{\epsilon}-\delta\tau_{\mathcal{P}}(\mathbf{h}),\mathbf{h}\right]+\cdots.$$

Here we have used (4.3) for $\tau_{\mathcal{P}_{\vec{\mathbf{y}}}}(\mathbf{h})$ and written explicitly the $O(1/\epsilon)$ terms. The first term vanishes as before at the correct speed, but the second term is $O(1/\epsilon)$ independent of $\tilde{c}_o$ (recall (4.4)). ∎

The annihilator introduced in Definition 4.1 works well in ideal situations for perfectly layered structures. This is seen clearly in the numerical simulations presented in section 6. We also study there the more complicated problem of a layered structure with additional isotropic fluctuations of the wave speed, due to small inhomogeneities. In that case, Definition 4.1 is not the best choice of an annihilator because the derivative over the offset h can amplify significantly the correlated "noise" due to the isotropic clutter. We propose the following alternative.

DEFINITION 4.3. *Consider a trial speed $\tilde{c}_o$, and let $T_{\tilde{c}_o}$ and $\zeta_{\tilde{c}_o}$ be as in Definition 4.1. Let also $\mathbf{h}' = \mathbf{h} + \xi\mathbf{e_h}$ be offsets collinear with $\mathbf{h} = h\mathbf{e_h}$, for ξ belonging to an interval $I(h)$ of length $|I(h)|$, limited by the constraint $\vec{\mathbf{x}}_s + (\mathbf{h}', 0) \in \mathcal{A}$. The filtering operator is given by*

(4.10)
$$[\mathbb{Q}_{\tilde{c}_o}D](t,\mathbf{h}) = \left\{D\left(T_{\tilde{c}_o}(h,z),\mathbf{h}\right) - \frac{1}{|I(h)|}\int_{I(h)} D\left(T_{\tilde{c}_o}(h+\xi,z),(h+\xi)\mathbf{e_h}\right)d\xi\right\}_{z=\zeta_{\tilde{c}_o}(h,t)}.$$

The first and last steps involved in (4.10) are the same as in Definition 4.1; it is the annihilation step that is different. Instead of taking derivatives with respect to the offset as in (4.8), we subtract the average of the traces with respect to the offset, after the normal move-out.

We omit the analysis of (4.10) because it is very similar to that in Lemma 4.2. We find that the annihilation of the coherent, strong layer echoes occurs for both small and large interval lengths $|I(h)|$. In the numerical simulations in section 6.2.4 we implement Definition 4.3 using the longest intervals $I(h)$, consistent with the constraint $\vec{\mathbf{x}}_s + (\mathbf{h}', 0) \in \mathcal{A}$, to average out the isotropic clutter effects. However, the choice of $I(h)$ affects significantly the influence of $\mathbb{Q}_{\tilde{c}_o}$ on the incoherent field $\mathcal{N}(t,\mathbf{h})$, which is backscattered by the randomly layered medium. The annihilation of $\mathcal{N}(t,\mathbf{h})$ is studied in [27], and it is shown there that $|I(h)|$ must be $O(\lambda_o)$ for the annihilation to be effective.

[2]These paths are "stronger" than those that scatter in the layered medium because of the following: (1) Each scattering at an interface reduces the amplitude of the echoes by multiplication with the reflection coefficient. (2) The longer the path is, the more it is affected by geometrical spreading and the ODA diffusion kernel due to the random medium.

4.2. Variable Background. Definitions 4.1 and 4.3 extend to the case of variable backgrounds in an obvious manner. Instead of (4.5) we take $T_{\tilde{c}}(h,z)$ to be the travel time of a primary reflection at depth $z<0$ in the medium with trial speed $\tilde{c}(z)$. This follows from Appendix A,

$$T_{\tilde{c}}(h,z) = 2\int_{-|z|}^{0} \frac{\sqrt{1-\tilde{c}^2(s)K_{\tilde{c}}^2}}{\tilde{c}(s)}ds + hK_{\tilde{c}}, \tag{4.11}$$

with horizontal slowness $K_{\tilde{c}}$ given by

$$\frac{h}{2} = K_{\tilde{c}}\int_{-|z|}^{0} \frac{\tilde{c}(s)}{\sqrt{1-\tilde{c}^2(s)K_{\tilde{c}}^2}}ds. \tag{4.12}$$

Note that because the right-hand side is monotonically increasing with $K_{\tilde{c}}$, we have a unique slowness satisfying condition (4.12) and, therefore, a unique $T_{\tilde{c}}(h,z)$ for each z. Furthermore, $T_{\tilde{c}}(h,z)$ increases monotonically[3] with $|z|$, so the inverse function $\zeta_{\tilde{c}}(t,h)$ satisfying

$$T_{\tilde{c}}\left(h,\zeta_{\tilde{c}}(h,t)\right) = t, \quad \zeta_{\tilde{c}}\left(h,T_{\tilde{c}}(h,z)\right) = z, \tag{4.13}$$

is also uniquely defined.

The annihilator operators are as in Definitions 4.1 and 4.3, with $T_{\tilde{c}}(h,z)$ used for the normal move-out and $\zeta_{\tilde{c}}(t,h)$ for the mapping between depths z and time t. The performance of the annihilators is expected to be worse than in the homogeneous case, because the multiple paths do not map exactly to primaries from ghost layers (i.e., L_{ghost} independent of h) at the correct speed. The degradation in performance depends on how much $c(z)$ varies along the multiple paths and on the depth where the stronger variations occur. We show with numerical simulations in section 6 that when the variations of $c(z)$ are not too large, the annihilation of the multiples is almost as good as in the homogeneous case.

5. Imaging and Velocity Estimation. We now use the layer annihilators for imaging the compactly supported reflectivity and for velocity estimation. We begin in section 5.1 with migration-type imaging. Then, we discuss CINT imaging in section 5.3.

5.1. Migration Imaging with Layer Annihilators. Under the idealization of a continuum array aperture, we define the migration imaging function with the annihilated data,[4]

$$\mathcal{J}(\vec{\mathbf{y}}^s;\tilde{c}) = \int_{\mathcal{A}} d\mathbf{h}\left[\mathbb{Q}_{\tilde{c}}D\right]\left(\tau(\vec{\mathbf{x}}_s,\vec{\mathbf{y}}^s,(\mathbf{x}_s+\mathbf{h},0)),\mathbf{h}\right). \tag{5.1}$$

Here $\mathbb{Q}_{\tilde{c}}$ is one of the annihilators introduced in section 4 for a trial speed $\tilde{c}(z)$, and $\tau(\vec{\mathbf{x}}_s,\vec{\mathbf{y}}^s,\vec{\mathbf{x}}_s+(\mathbf{h},0))$ is the travel time computed at the trial speed between the source at $\vec{\mathbf{x}}_s=(\mathbf{x}_s,0)$, the image point at $\vec{\mathbf{y}}^s$, and the receiver at $(\mathbf{x}_s+\mathbf{h},0)$.

[3] It follows from (4.11) and (4.12) that $\partial T_{\tilde{c}}/\partial|z| = 2/\tilde{c}(z)\sqrt{1-\tilde{c}^2(z)K_{\tilde{c}}^2} > 0$, with $z=-|z|$.

[4] The continuum approximation made in (5.1) is to be understood in practice as having a very dense array of sensors. This is in fact required in Definition 4.1 to approximate derivatives in offset. Definition 4.3 makes sense for receivers that are further apart, as well, in which case the integral over $\mathbf{h}$ in (5.1) should be replaced by a sum over the receivers.

As we have seen in section 4, the layer annihilators suppress the echoes from the layers above the reflectivity support $\mathcal{S}$ if the trial speed $\tilde{c}(z)$ is close to the true one. Take, for example, the annihilator in Definition 4.1 and use (4.11) and (4.12) to deduce that the primary arrival times satisfy

$$\frac{d}{dh}T_{\tilde{c}}(h,z) = K_{\tilde{c}}, \tag{5.2}$$

with horizontal slowness $K_{\tilde{c}}$ given by (4.12) or, equivalently, by

$$K_{\tilde{c}} = \mathbb{K}_{\tilde{c}}\left[T_{\tilde{c}}(h,z)\right]. \tag{5.3}$$

The map $\mathbb{K}_{\tilde{c}}$ cannot be written explicitly in general, unless we are in the homogeneous case $\tilde{c}(z) = \tilde{c}_o$, where

$$K_{\tilde{c}_o} = \frac{h}{\tilde{c}_o\sqrt{h^2+4z^2}} = \frac{h}{\tilde{c}_o^2 T_{\tilde{c}_o}(h,z)} = \mathbb{K}_{\tilde{c}_o}\left[T_{\tilde{c}_o}(h,z)\right]. \tag{5.4}$$

It is nevertheless unambiguously defined, as explained in section 4.2.

We have from (3.22), (5.1)–(5.3), and Definition 4.1 that

$$\begin{aligned}\mathcal{J}(\vec{\mathbf{y}}^s;\tilde{c}) = \sum_{\mathcal{P}}\int_{\mathcal{A}}\frac{d\mathbf{h}}{\epsilon}\left\{\mathbb{K}_{\tilde{c}}\left[\tau(\vec{\mathbf{x}}_s,\vec{\mathbf{y}}^s,(\mathbf{x}_s+\mathbf{h},0))\right] - \frac{d}{dh}\tau_{\mathcal{P}}(\mathbf{h})\right\}\\ \times\frac{\partial}{\partial t}\Phi_{\mathcal{P}}\left[\frac{\tau(\vec{\mathbf{x}}_s,\vec{\mathbf{y}}^s,(\mathbf{x}_s+\mathbf{h},0))}{\epsilon} - \frac{\tau_{\mathcal{P}}(\mathbf{h})}{\epsilon} - \delta\tau_{\mathcal{P}}(\mathbf{h}),\mathbf{h}\right] + \cdots,\end{aligned} \tag{5.5}$$

where we denote by the dots the lower order terms. We have computed already the derivatives

$$\frac{d}{dh}\tau_{\mathcal{P}_j}(\mathbf{h}) = \frac{d}{dh}T_c(h,L_j) = \mathbb{K}_c\left[\tau_{\mathcal{P}_j}(\mathbf{h})\right] \tag{5.6}$$

for the primary paths $\mathcal{P}_j$. For the other paths we write

$$\frac{d}{dh}\tau_{\mathcal{P}}(\mathbf{h}) = \mathbb{K}_c\left[\tau_{\mathcal{P}}(\mathbf{h})\right] + \psi_{\mathcal{P}}(\mathbf{h}), \quad \mathcal{P}\neq\mathcal{P}_j, \quad j=1,\ldots,M, \tag{5.7}$$

where the remainder $\psi_{\mathcal{P}}(\mathbf{h})$ may be $O(1)$, independent of the trial speed $\tilde{c}$.

REMARK 5.1. *In the most favorable case $c(z)=c_o$, the remainder $\psi_{\mathcal{P}}(\mathbf{h})$ vanishes for all paths that do not scatter in the reflectivity support $\mathcal{S}$, when $\tilde{c}=c_o$. However, the remainder does not vanish for paths $\mathcal{P}_{\vec{\mathbf{y}}}$ that involve scattering at points $\vec{\mathbf{y}}$ in the reflectivity support $\mathcal{S}$ (see Lemma 4.2). In the general case of variable $c(z)$, the remainder $\psi_{\mathcal{P}}(\mathbf{h})$ does not vanish for the multiple paths. However, it can be small if the variations of $c(z)$ are not too significant, as illustrated with numerical simulations in section 6.*

Returning to (5.5), and using (5.6), we obtain

$$\begin{aligned}\mathcal{J}(\vec{\mathbf{y}}^s;\tilde{c}) = \sum_{\mathcal{P}}\int_{\mathcal{A}}\frac{d\mathbf{h}}{\epsilon}\left\{\mathbb{K}_{\tilde{c}}\left[\tau(\vec{\mathbf{x}}_s,\vec{\mathbf{y}}^s,(\mathbf{x}_s+\mathbf{h},0))\right] - \mathbb{K}_c\left[\tau_{\mathcal{P}}(\mathbf{h})\right] + \psi_{\mathcal{P}}(\mathbf{h})\right\}\\ \times\frac{\partial}{\partial t}\Phi_{\mathcal{P}}\left[\frac{\tau(\vec{\mathbf{x}}_s,\vec{\mathbf{y}}^s,(\mathbf{x}_s+\mathbf{h},0))}{\epsilon} - \frac{\tau_{\mathcal{P}}(\mathbf{h})}{\epsilon} - \delta\tau_{\mathcal{P}}(\mathbf{h}),\mathbf{h}\right] + \cdots.\end{aligned} \tag{5.8}$$

Since $\Phi_{\mathcal{P}}$ has $O(1)$ support, we get a large $O(1/\epsilon)$ contribution at the image point $\vec{\mathbf{y}}^s$ if there is a path $\mathcal{P}$ for which

$$\tau(\vec{\mathbf{x}}_s,\vec{\mathbf{y}}^s,(\mathbf{x}_s+\mathbf{h},0)) = \tau_{\mathcal{P}}(\mathbf{h}) + O(\epsilon).$$

Each such path is weighted in (5.8) by the amplitude

$$\mathbb{K}_{\tilde{c}}\left[\tau(\vec{\mathbf{x}}_s,\vec{\mathbf{y}}^s,(\mathbf{x}_s+\mathbf{h},0))\right]-\mathbb{K}_c\left[\tau_{\mathcal{P}}(\mathbf{h})\right]+\psi_{\mathcal{P}}(\mathbf{h})\approx\mathbb{K}_{\tilde{c}}\left[\tau_{\mathcal{P}}(\mathbf{h})\right]-\mathbb{K}_c\left[\tau_{\mathcal{P}}(\mathbf{h})\right]+\psi_{\mathcal{P}}(\mathbf{h}).$$

The first two terms on the right-hand side are the horizontal slownesses at speeds $\tilde{c}$ and c, respectively. They cancel each other when the trial speed is right, and then the image is determined by the paths with remainder $\psi_{\mathcal{P}} = O(1)$. As stated in Remark 5.1, all paths that scatter at the reflectivity in $\mathcal{S}$ have a large remainder. We have now shown the main result.

PROPOSITION 5.2. *Assuming a homogeneous background c_o and a trial speed $\tilde{c}_o = c_o+O(\epsilon)$, the migration imaging function* (5.1) *peaks in the support $\mathcal{S}$ of the reflectivity and not at the layers above it. If the trial speed $\tilde{c}_o$ is not close to c_o, the top layers in the structure obscure the reflectivity. If the background is not homogeneous, but the trial speed is right, the annihilator partially obscures the top layers by eliminating the contribution of the primary paths $\mathcal{P}_j$ in the image.*

5.2. Algorithm for Imaging and Velocity Estimation with Layer Annihilators. Using Proposition 5.2 we can formulate the following algorithm for imaging jointly with velocity estimation:

1. Choose a trial speed $\tilde{c}(z)$.
2. Form the image (5.1) at points $\vec{\mathbf{y}}^s$ in the search domain $\mathcal{S}^s$, using the data filtered by the layer annihilator $\mathbb{Q}_{\tilde{c}}$. The search domain is assumed to contain $\mathcal{S}$, the unknown support of the reflectivity.
3. Compute the objective function

$$\mathcal{F}(\tilde{c})=\frac{|\mathcal{J}(\vec{\mathbf{y}}^s;\tilde{c})|_{L^1(\mathcal{S}^s)}}{\max\limits_{\vec{\mathbf{y}}^s\in\mathcal{S}^s}|\mathcal{J}(\vec{\mathbf{y}}^s;\tilde{c})|}. \tag{5.9}$$

4. Adjust the speed $\tilde{c}$ using optimization over a compact set C of admissible speeds:

$$\min_{\tilde{c}\in C}\mathcal{F}(\tilde{c}). \tag{5.10}$$

This algorithm returns a speed $\tilde{c}(z)$ that produces an image of small spatial support, as measured by the sparsity promoting L^1 norm in the objective function (5.9). It is expected to work well when imaging scatterers of small support $\mathcal{S}$, because the images at incorrect speeds are dominated by the top layers, which involve more pixels in the image than those contained in $\mathcal{S}$.

REMARK 5.3. *We can simplify the optimization by taking the L^2 norm in* (5.9) *and replacing the division by the maximum of $\mathcal{J}$ with an equality constraint. The L^1 norm should be better in theory for getting a sharper image, but we have not seen a significant difference in our numerical simulations.*

REMARK 5.4. *As an alternative algorithm for velocity estimation, we can seek $\tilde{c}(z)$ as the minimizer of the L^2 norm of the annihilated data traces*

$$\int_{\mathcal{A}}d\mathbf{h}\int dt\,\left|\left[\mathbb{Q}_{\tilde{c}}D\right](t,\mathbf{h})\right|^2. \tag{5.11}$$

5.3. CINT Imaging with Layer Annihilators. CINT imaging was introduced in [31] for mitigating the correlated "noise" due to clutter in the medium. It involves

a statistical smoothing process that takes cross-correlations of the data traces over carefully chosen windows. The CINT imaging function with unfiltered data is

$$\mathcal{J}^{\rm CINT}(\vec{\mathbf{y}}^s;\tilde{c}) = \int d\omega \int_{\mathcal{A}} d\mathbf{h} \int d\tilde{\omega}\ \hat{\chi}_t\left(\tilde{\omega};\Omega_d\right) \int d\tilde{\mathbf{h}}\, \hat{\chi}_{\mathbf{h}}\left(\frac{\omega}{\epsilon}\tilde{\mathbf{h}};\kappa_d^{-1}\right) \times \hat{D}\left(\frac{\omega}{\epsilon}+\frac{\tilde{\omega}}{2\epsilon},\mathbf{h}+\frac{\tilde{\mathbf{h}}}{2}\right)\overline{\hat{D}\left(\frac{\omega}{\epsilon}-\frac{\tilde{\omega}}{2\epsilon},\mathbf{h}-\frac{\tilde{\mathbf{h}}}{2}\right)} \exp\left\{-i\left(\frac{\omega}{\epsilon}+\frac{\tilde{\omega}}{2\epsilon}\right)\tau\left(\vec{\mathbf{x}}_s,\vec{\mathbf{y}}^s,(\mathbf{x}_s+\mathbf{h}+\tilde{\mathbf{h}}/2,0)\right) + i\left(\frac{\omega}{\epsilon}-\frac{\tilde{\omega}}{2\epsilon}\right)\tau\left(\vec{\mathbf{x}}_s,\vec{\mathbf{y}}^s,(\mathbf{x}_s+\mathbf{h}-\tilde{\mathbf{h}}/2,0)\right)\right\}.$$

Here we denote by $\hat{D}$ the Fourier transform of the data with respect to time and we scale the frequency by $1/\epsilon$, as explained in section 3.2. We use the window $\hat{\chi}_t(\cdot,\Omega_d)$ to restrict the scaled frequency offset $\tilde{\omega}$ by Ω_d, and we limit $|\tilde{\mathbf{h}}| \le \frac{\epsilon}{\omega\kappa_d}$ with the window $\hat{\chi}_{\mathbf{h}}\left(\frac{\omega}{\epsilon}\cdot;\kappa_d^{-1}\right)$. The bar in $\mathcal{J}^{\rm CINT}(\vec{\mathbf{y}}^s)$ stands for the complex conjugate of $\hat{D}$.

CINT images by migrating the cross-correlations of the data with the travel times computed in the smooth medium with speed $\tilde{c}(z)$. The supports Ω_d and κ_d^{-1} of the windows $\hat{\chi}_t$ and $\hat{\chi}_{\mathbf{h}}$ must be chosen carefully to get good results. To see this, we note that straightforward calculations (see [30, 33]) let us rewrite the equation above as

$$\mathcal{J}^{\rm CINT}(\vec{\mathbf{y}}^s;\tilde{c}) \approx \int_{\mathcal{A}} d\mathbf{h} \int d\omega \int d\mathbf{K} \int dt\, W(\omega,\mathbf{K},t,\mathbf{h}) \times \chi_t\left(\frac{\tau(\vec{\mathbf{x}}_s,\vec{\mathbf{y}}^s,(\mathbf{x}_s+\mathbf{h},0))-t}{\epsilon};\Omega_d^{-1}\right)\chi_{\mathbf{h}}\left(\nabla_{\mathbf{h}}\tau(\vec{\mathbf{x}}_s,\vec{\mathbf{y}}^s,(\mathbf{x}_s+\mathbf{h},0))-\mathbf{K};\kappa_d\right), \tag{5.12}$$

in terms of the Wigner transform of the data

$$W(\omega,\mathbf{K},t,\mathbf{h}) = \int d\tilde{t}\int d\tilde{\mathbf{h}}\,\hat{D}\left(\frac{\omega}{\epsilon}+\frac{\tilde{\omega}}{2\epsilon},\mathbf{h}+\frac{\tilde{\mathbf{h}}}{2}\right)\overline{\hat{D}\left(\frac{\omega}{\epsilon}-\frac{\tilde{\omega}}{2\epsilon},\mathbf{h}-\frac{\tilde{\mathbf{h}}}{2}\right)}e^{i\frac{\omega}{\epsilon}(\tilde{t}-\tilde{\mathbf{h}}\cdot\mathbf{K})}. \tag{5.13}$$

Note how the windows χ_t and $\chi_{\mathbf{h}}$ are used in (5.12) for smoothing the Wigner transform. Such smoothing is essential for getting statistically stable results that are independent of the realization of the clutter [33]. CINT imaging is a trade-off between smoothing for stability and minimizing the image blur. The range blur is inversely proportional to Ω_d, and the cross-range blur is proportional to κ_d, the support of window $\chi_{\mathbf{h}}$. The parameter Ω_d is the decoherence frequency and κ_d is the uncertainty in the horizontal slowness. They both depend on the statistics of the random medium, which is typically unknown. However, we can determine them adaptively, with optimization of the image that they produce, as shown in [30].

The results in [30] apply to a smooth medium cluttered by small inhomogeneities. In this paper we have the additional layered structure that creates strong echoes at the array. We deal with these echoes by replacing the data in (5.12) with the filtered data $[\mathbb{Q}_{\tilde{c}}D](t,\mathbf{h})$. The velocity estimation can then be done jointly with CINT imaging, by using an algorithm analogous to that in section 5.1.

REMARK 5.5. *The ODA theory used in this paper says that simple migration of the annihilated data should give very good results in layered media. This is an asymptotic result in the limit $\epsilon \to 0$. In practice we find that migration images can be*

noisy and that they can be improved with adaptive CINT imaging, as noted in [32] *and section* 6. *The use of CINT imaging simplifies in layered media because there is no spatial decoherence in the data, i.e., no uncertainty over the horizontal slowness. It is only the smoothing over arrival times that affects the results, and even this smoothing is not dramatic. The adaptive algorithm returns an* $O(1)$ *value of* Ω_d, *which makes the range resolution of order* ϵ, *as in ideal migration. In layered media with additional fluctuations of the speed due to small, isotropic inhomogeneities, smoothing over the horizontal slowness is typically needed.*

6. Numerical Simulations. We present numerical simulations for migration and CINT imaging in layered media. We show by comparison with the simpler problem of imaging sources that backscattering is a serious issue when imaging scatterers buried deep in layered structures. We then illustrate the beneficial effect of layer annihilators on the imaging process.

The array data is generated by solving (3.1) in two dimensions, with the mixed finite element method described in [14, 15]. The infinite extent of the medium is modeled numerically with a perfectly matched absorbing layer surrounding the computational domain.

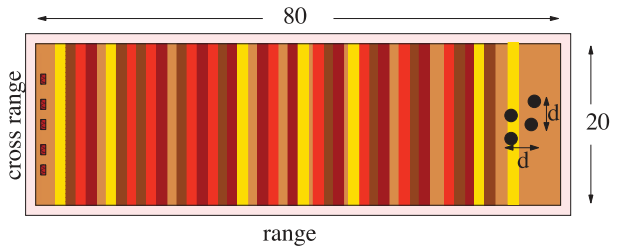

Fig. 6.1 *Setup for numerical simulations with sources buried in a finely layered structure. The units are in carrier wavelengths* λ_o *and the distance* d *between the scatterers is* 4. *The perfectly matched layer surrounding the domain is shown in pink.*

6.1. Sources Buried in Finely Layered Structures. The setup for the simulations with sources buried in layered media is shown in Figure 6.1. We use an array of 41 receivers at distance $\lambda_o/2$ apart from each other. The sources are at depth $L \sim 78\lambda_o$. The wave speed is plotted on the left in Figure 3.2. It fluctuates around the constant value $c_o = 3\text{km/s}$. The source has directivity along the z axis and it emits the pulse $f(t)$ given by the derivative of a Gaussian. While everything is scaled in terms of the central wavelength, we choose for illustration numbers that are typical in exploration geophysics. We let $\omega_o/(2\pi) = 30\text{Hz}$ be the central frequency, so that $\lambda_o = 100\text{m}$ and $L = 7.8\text{km}$. The bandwidth is $B = 20 - 40\text{Hz}$ (measured at 6dB) and the correlation length is $\ell = 10\text{m}$.

We show in Figure 6.2 the data traces for one and four sources buried in the layered medium. The time axis is scaled by the pulse width, which is 0.02s in our simulations, and the cross-range is scaled by the central wavelength. We note in Figure 6.2 the strong coherent arrivals of the signals from the sources and the trail of weaker incoherent echoes from the finely layered structure. The Kirchhoff migration and CINT images with these data are shown in Figure 6.3. Although in theory migration should work well, we see how the smoothing in CINT imaging improves the images, especially in the case of four sources.

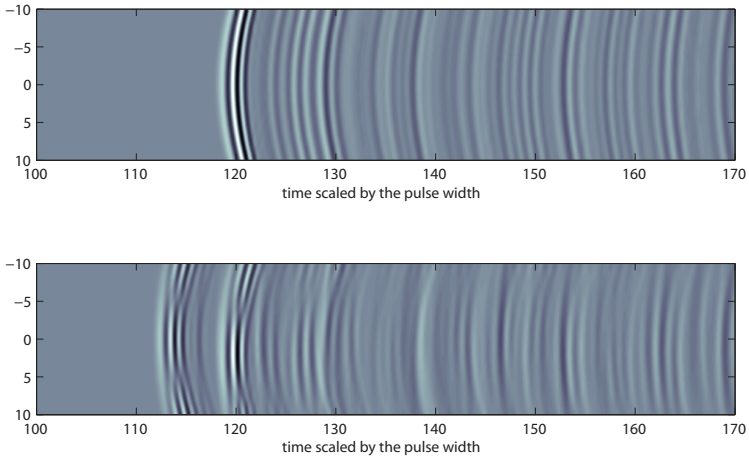

Fig. 6.2 *Traces recorded at the array for a single source (top) and four sources (bottom). The pulse width is* 0.02s.

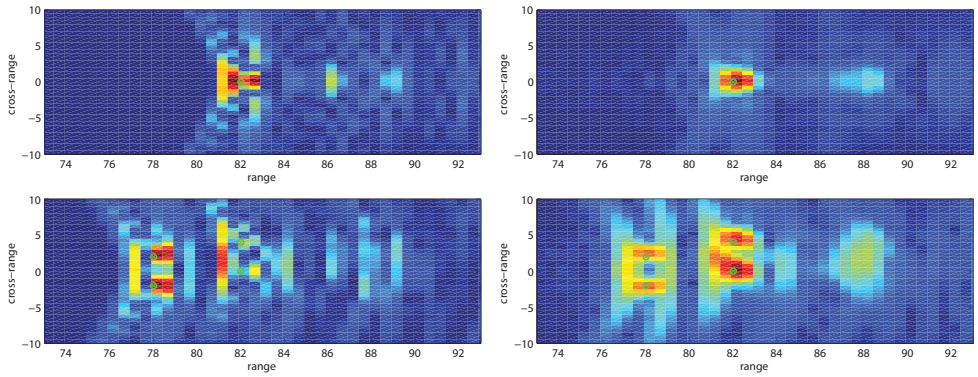

Fig. 6.3 *Top: Images with the traces in Figure* 6.2 *(top) for a single source. Bottom: Images with the traces in Figure* 6.2 *(bottom) for four point sources. Left column: Kirchhoff migration. Right column: CINT imaging. The correct location of the source is shown in each figure with a dot.*

6.2. Scatterers Buried in Finely Layered Structures. We present numerical simulations for layered media with constant and variable background speeds. We also consider media with isotropic clutter in addition to the layered structure.

6.2.1. Simulations for a Constant Background Speed. Consider first the simulation with the setup shown in Figure 3.3. The source is now at the center point in the array and it emits the same pulse as before, with central frequency $\omega_o/(2\pi) = 30$Hz and bandwidth 20–40Hz. The array has 81 receivers distributed uniformly over the aperture $a = 40\lambda_o$. The wave speed $v(z)$ is as in Figure 3.3. It has a constant part $c_o = 3$km/s, rapid fluctuations with correlation length $\ell = 0.02\lambda_o = 2$m, and five strong blips (interfaces) separated by distance $10\lambda_o = 1$km. The reflectivity $\nu(\vec{\mathbf{x}})$ is supported on three soft acoustic scatterers (i.e., pressure is zero at their boundary)

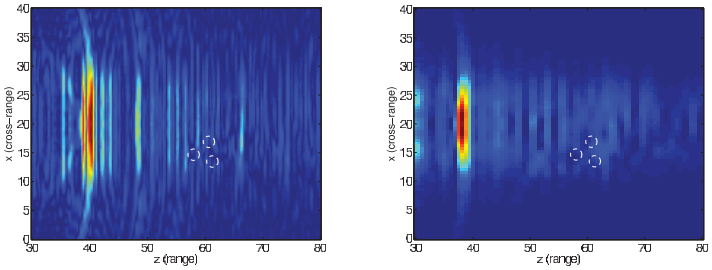

Fig. 6.4 *Images with the traces in Figure* 3.3. *Kirchhoff migration is on the left and CINT imaging on the right. The small scatterers are indicated with circles and they are invisible in both images. Both range and cross-range are scaled by* λ_o.

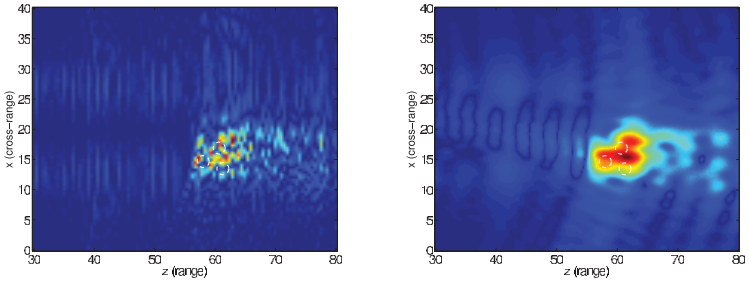

Fig. 6.5 *Images with filtered data* $[\mathbb{Q}_{c_o} D](t,h)$. *Migration is on the left and CINT imaging on the right.*

that are disks of radius λ_o. They are at depth $L \sim 60\lambda_o = 6$km and at distance $2.5\lambda_o = 250$m apart. Note that the setup is in agreement with assumption (3.18) of separation of scales, for $\epsilon = 0.02$, because

$$\frac{\ell}{\lambda_o} = 0.02 \sim \frac{\lambda_o}{L} = 0.017.$$

The change in $v(z)$ at the interfaces is close to 100% and the rapid fluctuations have an amplitude of 10%.

The data traces are shown in Figure 3.3. The reflectivity is masked by the layered structure above it, and it cannot be seen with migration or CINT imaging (see Figure 6.4).

The results improve dramatically when imaging with filtered data $[\mathbb{Q}_{c_o} D](t,h)$ at the true speed c_o, as shown in Figure 6.5. The annihilators in Definitions 4.1 and 4.3 give similar results in this case, so we show only the plots for the first one. Note that the scatterers are too close together to be resolved by migration or CINT imaging. The images could be improved in principle if we had more data (more source locations), using optimal subspace projections as in [34]. We will consider such improvements in a separate publication.

In Figure 6.6 we illustrate the estimation of the background speed $\tilde{c}_o$ using the layer annihilators. We form the image with migration of the filtered data $[\mathbb{Q}_{\tilde{c}_o} D](t,h)$, and we plot its L^2 norm computed in the same domain as in Figures 6.4–6.5. Note the monotone behavior of the objective function near the optimum $\tilde{c}_o = c_o$. The

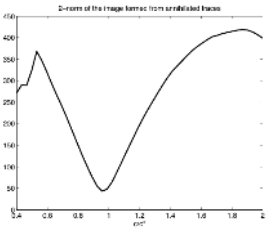

Fig. 6.6 *Plot of the L_2 norm of the image, as a function of the trial speed $\tilde{c}_o$.*

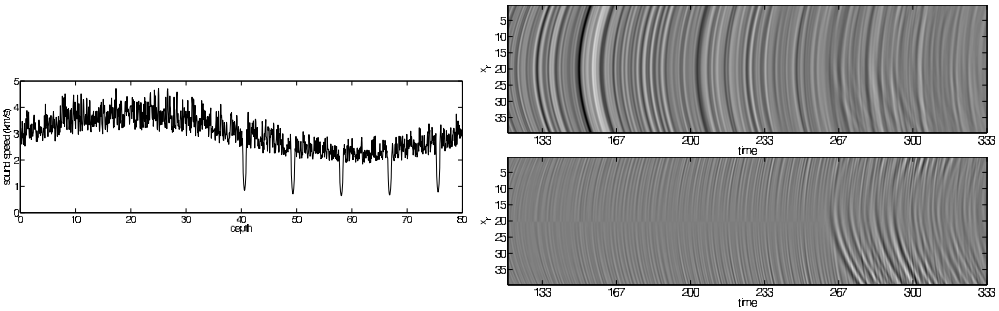

Fig. 6.7 *Left: Wave speed $v(z)$. Right: Traces before (top) and after (bottom) annihilation. The time axis is scaled by the pulse width and the receiver location is scaled by λ_o. The echoes from the small scatterers are overwhelmed by those from the layers in the top traces, but they are clearly emphasized after the annihilation.*

decrease noted at the ends of the trial speed interval is to be discarded, as it is due to $\tilde{c}_o$ being so wrong that the image peaks are pushed outside the image domain fixed in the optimization.

6.2.2. Simulations for a Variable Background Speed. In the next simulation we consider the variable background speed shown in Figure 6.7 on the left. All other parameters are the same as in section 6.2.1. We compute the travel times $T_c(h, z)$ by essentially solving (4.11)–(4.12). The actual implementation uses the MATLAB Toolbox Fast Marching [61], which computes the viscosity solution of the eikonal equation using level sets and the fast marching algorithm.

We plot on the right in Figure 6.7 the traces before and after annihilation. Note the emergence of the echoes from the small scatterers after the annihilation. The images with the annihilated data are similar to those in Figure 6.5, so we do not include them in this paper.

Let us now take a finely layered medium with the speed as in Figure 6.7 but without the five strong blips. The traces and the Kirchhoff migration image are shown in Figure 6.8 on the left. We see that the layered medium impedes the imaging process even in the absence of the strong interfaces. The echoes due to the layered structure are now just the incoherent ones denoted by $\mathcal{N}(t, \mathbf{h})$ in (3.22). We do not present in this paper any theory for the annihilation of such incoherent echoes; this is done in a different publication [27]. However, we illustrate with numerical results on the right in Figure 6.8 the enhancement of the signal from the compact scatterers and the significant improvement of the migration image obtained with layer annihilation.

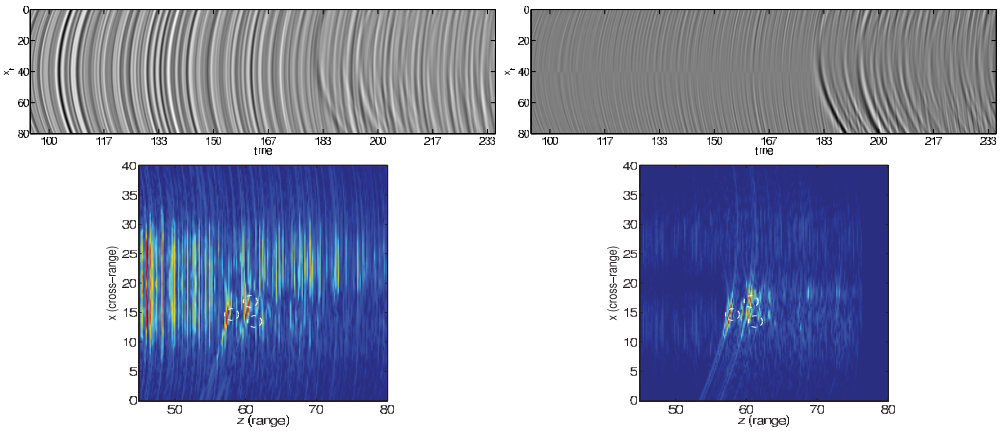

Fig. 6.8 *Left: Traces and Kirchhoff migration image without annihilation. Right: Annihilated traces and the resulting migration image. The speed $v(z)$ is as in Figure* 6.7 *but without the five strong scattering interfaces.*

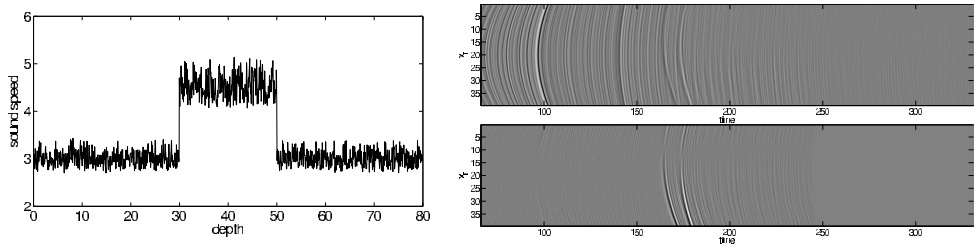

Fig. 6.9 *Left: Wave speed $v(z)$. Right: Traces before (top) and after (bottom) annihilation.*

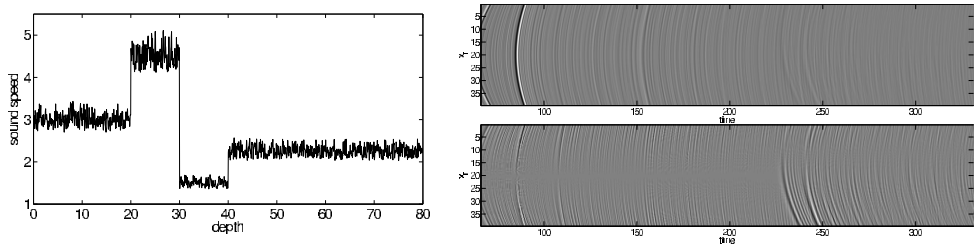

Fig. 6.10 *Left: Wave speed $v(z)$. Right: Traces before (top) and after (bottom) annihilation.*

6.2.3. Simulations for Media with Discontinuous Background Speeds. We illustrate here the performance of the layer annihilators in the case of background speeds $c(z)$ with jump discontinuities. We show in Figures 6.9–6.10 the results of two simulations. The wave speed $v(z)$ is plotted on the left, and the traces before and after annihilation are shown on the right. The filters $\mathbb{Q}_c$ are defined at the true mean speed. The coherent echoes from the reflectors that we wish to image are seen clearly in the filtered traces in Figures 6.9–6.10 but not in the raw, measured traces.

6.2.4. Simulations for Layered Media with Additional Isotropic Clutter. In our last simulation we return to the setup considered in section 6.2.1 and add isotropic clutter to the medium. This is modeled with a random process generated with random

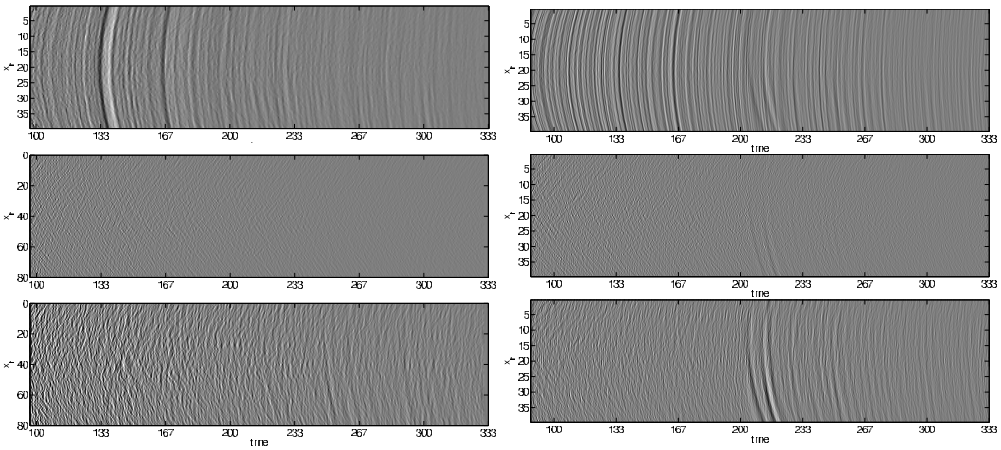

Fig. 6.11 *Top: Raw traces for the layered structure plotted in Figure* 3.3 *and additional isotropic clutter. Middle: Traces filtered with the annihilator in Definition* 4.1. *Bottom: Traces filtered with the annihilator in Definition* 4.3. *Left: Isotropic clutter with* 3% *standard deviation. Right: Isotropic clutter with* 1% *standard deviation.*

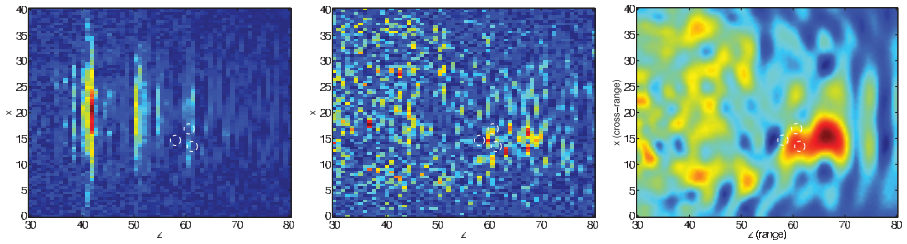

Fig. 6.12 *Left: Migration image with the raw traces shown on the top in Figure* 6.11. *Middle: Migration with the annihilated traces shown on the bottom left in Figure* 6.11. *Right: CINT image with the annihilated traces shown on the bottom left in Figure* 6.11.

Fourier series. We take a Gaussian correlation function, with correlation length equal to λ_o. The standard deviation of the isotropic fluctuations of the wave speed is 3%.

We show in Figure 6.11 the traces before and after filtering with the annihilators $\mathbb{Q}_{c_o}$ given by Definitions 4.1 and 4.3. We plot for comparison the traces for both 3% and 1% standard deviation of the isotropic clutter. We note that the first choice does not work well, in the sense that it magnifies the effect of the isotropic clutter at the early times. This is due to the offset derivative in Definition 4.1. The layer annihilator given by Definition 4.3 works much better, as seen in the bottom plots of Figure 6.11. The emergence of the echoes from the small scatterers is seen more clearly in the weaker clutter (bottom right plot in Figure 6.11).

Before the annihilation we can image only the top two strong scattering interfaces (left plot in Figure 6.12). After the annihilation, we can image below these interfaces. However, we still have to deal with the loss of coherence of the echoes due to scattering by the isotropic clutter. This makes the migration image speckled and difficult to interpret, as seen in the middle plot in Figure 6.12. The speckles are suppressed in the CINT image (right plot in Figure 6.12) because of the statistical smoothing induced by the cross-correlation of the annihilated traces in appropriately sized time and offset

windows (see section 5 and [31, 30, 33]). The CINT image in Figure 6.12 is obtained with the decoherence frequency $\Omega_d = 3\%$ of the bandwidth and decoherence length $X_d = 15.9\lambda$. We note that the image peaks at the small scatterers and slightly behind them. This is because of the strong interface that lies just below the small scatterers (see Figure 3.3). The layer annihilator is not designed to suppress the echoes that have been multiply scattered between the small scatterers and the interfaces. These are coherent echoes that are not eliminated by the statistical smoothing in CINT imaging either, and this is why we see their effect in the image. We expect that the result could be improved if we had more data (more source locations), using optimal subspace projections as in [34]. We will consider such improvements in a separate publication.

7. Summary and Conclusions. The focus of this paper is on the use of data filtering operators, called layer annihilators, for imaging small scatterers buried deep in layered deterministic and random structures. The annihilators are designed to suppress the echoes from the layered structure and enhance the signals from the compact scatterers that we wish to image. We have shown analytically and with numerical simulations that the layer annihilators can significantly improve the images if we know the smooth part of the wave speed in the medium. This determines the kinematics (i.e., the travel times) of the data that we record with an array of sensors placed at the top of the layered structure.

If we compute travel times with the wrong background speed, then the annihilators do not suppress the echoes from the layer structure and the resulting images are bad. This is why we can also use the annihilators for velocity estimation. We have indicated briefly how to carry out velocity estimation jointly with imaging. This is done by optimizing an objective function that measures the quality of the image as it is being formed with data filtered with a trial background speed.

We note that the imaging methods discussed in this paper do not require any knowledge of the rough part of the background speed. This rough part may be due to strongly scattering interfaces or to fine layering at the subwavelength scale, which we model with random processes. We may also have additional isotropic clutter due to the presence of small inhomogeneities in the medium. We have shown that we can mitigate lack of knowledge of the rough part of the wave speed for the purpose of imaging, using the following: (1) layer annihilators for enhancement of the signals from the compact scatterer to be imaged, and (2) CINT imaging for stabilization of the images with a statistical smoothing process that involves cross-correlations of the annihilated data traces over carefully chosen time and source-receiver offset windows.

The analysis in this paper is concerned with the annihilation of the echoes coming from strongly scattering interfaces in the medium. These echoes dominate the coherent part of the wavefield as described by the O'Doherty–Anstey (ODA) theory. However, the numerical simulations indicate that the incoherent field that is backscattered by the random medium is annihilated as well. The analysis of this surprising phenomenon requires a deeper understanding of reflected signals from the fine layering, beyond the ODA theory [50]. It is presented in [27].

Appendix A. Derivation of the Scattering Series. We derive here the multiple scattering series (3.22) for the data recorded at the array. As explained in section 3.1, when using the Born approximation for scattering by the reflectivity $\nu(\vec{\mathbf{x}})$ supported in $\mathcal{S}$, we can reduce the problem to that of waves in purely layered media for a point source excitation. Specifically, the pressure field $p(t, \vec{\mathbf{x}})$ observed at the array for time $t < \tau^{\mathcal{S}}$, the travel time from the source at $\vec{\mathbf{x}}_s$ to the reflectivity support $\mathcal{S}$ and back,

satisfies the initial value problem

$$\begin{aligned} \rho\frac{\partial\vec{\mathbf{u}}}{\partial t}(t,\vec{\mathbf{x}}) + \nabla p(t,\vec{\mathbf{x}}) &= \vec{\mathbf{F}}(t,\vec{\mathbf{x}}),\\ \frac{1}{v^2(z)}\frac{\partial p}{\partial t}(t,\vec{\mathbf{x}}) + \rho\nabla\cdot\vec{\mathbf{u}}(t,\vec{\mathbf{x}}) &= 0, \quad \vec{\mathbf{x}}\in\mathbb{R}^d, \quad t>0,\\ \vec{\mathbf{u}}(t,\vec{\mathbf{x}}) = \vec{\mathbf{0}}, \quad p(t,\vec{\mathbf{x}}) &= 0, \quad t<0. \end{aligned} \tag{A.1}$$

The incident field $p^i(t,\vec{\mathbf{y}})$ on the reflectivity (see (3.7)) is also given by the solution of (A.1), evaluated at points $\vec{\mathbf{y}}\in\mathcal{S}$. Finally, (3.8) for the Green's function appearing in (3.7) is very similar to (A.1). Once we solve (A.1), we can deduce easily the result for $G(t,\vec{\mathbf{x}},\vec{\mathbf{y}})$ and, consequently, the series (3.22).

A.1. The Plane Wave Decomposition. It is convenient to analyze (A.1) in the phase space

$$\begin{aligned} \hat{p}\left(\frac{\omega}{\epsilon},\mathbf{K},z\right) &= \int dt\int d\mathbf{x}\, p(t,\mathbf{x},z)e^{i\frac{\omega}{\epsilon}(t-\mathbf{K}\cdot\mathbf{x})},\\ \hat{\vec{\mathbf{u}}}\left(\frac{\omega}{\epsilon},\mathbf{K},z\right) &= \int dt\int d\mathbf{x}\,\vec{\mathbf{u}}(t,\mathbf{x},z)e^{i\frac{\omega}{\epsilon}(t-\mathbf{K}\cdot\mathbf{x})}, \quad \vec{\mathbf{u}}=(\mathbf{u},u). \end{aligned} \tag{A.2}$$

Here we Fourier transform p and $\vec{\mathbf{u}}$ with respect to time t and the cross-range variables $\mathbf{x}\in\mathbb{R}^{d-1}$, where $\vec{\mathbf{x}}=(\mathbf{x},z)$. We scale the frequencies by $1/\epsilon$, as explained in section 3.2, and we let the dual variable to $\mathbf{x}$ in the plane wave decomposition be the slowness vector (with units of time over length) $\mathbf{K}\in\mathbb{R}^{d-1}$.

Let us eliminate $\hat{\mathbf{u}}$ from the Fourier transformed equations (A.1) and obtain for each random slab

$$\begin{aligned} \frac{i\omega}{\epsilon}\left[|\mathbf{K}|^2-\frac{1}{v^2(z)}\right]\hat{p}+\rho\frac{\partial\hat{u}}{\partial z} &= 0,\\ -\frac{i\omega}{\epsilon}\rho\hat{u}+\frac{\partial\hat{p}}{\partial z} &= 0, \quad -L_j<z<-L_{j-1}, \quad j=1,\ldots,M. \end{aligned} \tag{A.3}$$

This is a one-dimensional wave equation for plane waves propagating in the direction of $\mathbf{K}$ at speed $v(z)/\sqrt{1-v^2(z)|\mathbf{K}|^2}$. At $z=0$ we have the jump conditions

$$\begin{aligned} \hat{p}\left(\frac{\omega}{\epsilon},\mathbf{K},0^+\right)-\hat{p}\left(\frac{\omega}{\epsilon},\mathbf{K},0^-\right) &= \epsilon^{\frac{d+1}{2}}\hat{f}(\omega)e^{-i\frac{\omega}{\epsilon}\mathbf{K}\cdot\mathbf{x}_s},\\ \hat{u}\left(\frac{\omega}{\epsilon},\mathbf{K},0^+\right)-\hat{u}\left(\frac{\omega}{\epsilon},\mathbf{K},0^-\right) &= \frac{\epsilon^{\frac{d+1}{2}}\mathbf{K}\cdot\hat{\mathbf{F}}(\omega)}{\rho}e^{-i\frac{\omega}{\epsilon}\mathbf{K}\cdot\mathbf{x}_s}, \end{aligned} \tag{A.4}$$

due to the source excitation (3.10) at $\vec{\mathbf{x}}_s=(\mathbf{x}_s,0)$. The scattering interfaces at $z=-L_j$, for $j=1,\ldots,M$, are modeled later using transmission and reflection coefficients.

A.2. The Up- and Down-Going Waves. In order to study scattering in the layered medium, we decompose the wave field into up- and down-going waves. The decomposition is done separately in each random slab $-L_j<z<-L_{j-1}$, and then the fields are mapped between the slabs via scattering operators at the separation interfaces $z=-L_j$ for $j=1,\ldots,M$.

For the slab $-L_j < z < -L_{j-1}$ we write

$$\hat{p}\left(\frac{\omega}{\epsilon},\mathbf{K},z\right) = \frac{\sqrt{\gamma(K,z)}}{2}\left[\hat{\alpha}^\epsilon(\omega,\mathbf{K},z)e^{i\frac{\omega}{\epsilon}\tau_j(K,z)} - \hat{\beta}^\epsilon(\omega,\mathbf{K},z)e^{-i\frac{\omega}{\epsilon}\tau_j(K,z)}\right],$$

$$\hat{u}\left(\frac{\omega}{\epsilon},\mathbf{K},z\right) = \frac{1}{2\sqrt{\gamma(K,z)}}\left[\hat{\alpha}^\epsilon(\omega,\mathbf{K},z)e^{i\frac{\omega}{\epsilon}\tau_j(K,z)} + \hat{\beta}^\epsilon(\omega,\mathbf{K},z)e^{-i\frac{\omega}{\epsilon}\tau_j(K,z)}\right], \tag{A.5}$$

where α^ϵ and β^ϵ are the amplitudes of the up- and down-going waves. These amplitudes are random variables, but the remaining coefficients in (A.5) are deterministic. Explicitly,

$$\gamma(K,z) = \frac{\rho c(z)}{\sqrt{1-c^2(z)K^2}} \tag{A.6}$$

is the acoustic impedance of the plane waves propagating in the direction of $\mathbf{K}$ in the smooth background, at speed $c(z)/\sqrt{1-c^2(z)K^2}$, with $K=|\mathbf{K}|$. The exponents in (A.5) are the travel times computed in the smooth medium, relative to the top of the slab:

$$\tau_j(K,z) = \int_{-L_{j-1}}^{z} \frac{\sqrt{1-c^2(s)K^2}}{c(s)}ds. \tag{A.7}$$

Substituting (A.5) into (A.3), we obtain a coupled system of stochastic differential equations for α^ϵ and β^ϵ. We write these equations using the matrix valued propagator $\mathbb{P}_j^\epsilon(\omega,K,z)$, satisfying

$$\begin{aligned} \frac{\partial \mathbb{P}_j^\epsilon}{\partial z} &= \left[\frac{i\omega}{\epsilon}\mu\left(\frac{z}{\epsilon^2}\right)\frac{\gamma(K,z)}{2\rho c^2(z)}\mathbb{H}_j^\epsilon + \frac{\partial}{\partial z}\ln\sqrt{\gamma(K,z)}\mathbb{M}_j^\epsilon\right]\mathbb{P}_j^\epsilon, \\ \mathbb{P}_j^\epsilon &= I \quad \text{at } z=-L_j^+, \end{aligned} \tag{A.8}$$

with

$$\mathbb{H}_j^\epsilon = \begin{pmatrix} 1 & -e^{-2i\frac{\omega}{\epsilon}\tau_j(K,z)} \\ e^{2i\frac{\omega}{\epsilon}\tau_j(K,z)} & -1 \end{pmatrix} \quad \text{and} \quad \mathbb{M}_j^\epsilon = \begin{pmatrix} 0 & e^{-2i\frac{\omega}{\epsilon}\tau_j(K,z)} \\ e^{2i\frac{\omega}{\epsilon}\tau_j(K,z)} & 0 \end{pmatrix}.$$

The propagator $\mathbb{P}_j^\epsilon(\omega,K,z)$ maps the amplitudes at the bottom of the slab $z=-L_j^+$ to the amplitudes at an arbitrary depth z in the slab:

$$\begin{pmatrix} \hat{\alpha}^\epsilon(\omega,\mathbf{K},z) \\ \hat{\beta}^\epsilon(\omega,\mathbf{K},z) \end{pmatrix} = \mathbb{P}_j^\epsilon(\omega,K,z)\begin{pmatrix} \hat{\alpha}^\epsilon(\omega,\mathbf{K},-L_j^+) \\ \hat{\beta}^\epsilon(\omega,\mathbf{K},-L_j^+) \end{pmatrix}. \tag{A.9}$$

The boundary conditions at $z=-L_j^+$ are not known a priori and are to be determined recursively, as we explain in the following sections. We do know, however, the boundary conditions at the surface $z=0$, where the source and the array are

$$\alpha^\epsilon(\omega,\mathbf{K},0^+) = \alpha^\epsilon(\omega,\mathbf{K},0^-) + \frac{\epsilon^{\frac{d+1}{2}}e^{-i\frac{\omega}{\epsilon}\mathbf{K}\cdot\mathbf{x}_s}}{\sqrt{\gamma(K,0)}}\left[\hat{f}(\omega) + \frac{\gamma(K,0)}{\rho}\mathbf{K}\cdot\hat{\mathbf{F}}(\omega)\right], \tag{A.10}$$

$$\beta^\epsilon(\omega,\mathbf{K},0^-) = \frac{\epsilon^{\frac{d+1}{2}}e^{-i\frac{\omega}{\epsilon}\mathbf{K}\cdot\mathbf{x}_s}}{\sqrt{\gamma(K,0)}}\left[\hat{f}(\omega) - \frac{\gamma(K,0)}{\rho}\mathbf{K}\cdot\hat{\mathbf{F}}(\omega)\right]. \tag{A.11}$$

These equations follow from (A.4), (A.5), and identity

$$\beta^\epsilon(\omega, \mathbf{K}, 0^+) = 0, \tag{A.12}$$

which says that there are no down-going waves above the source in the homogeneous half space $z > 0$.

We refer to

$$\beta^\epsilon(\omega, \mathbf{K}, 0^-) = \frac{\epsilon^{\frac{d+1}{2}} \hat{\varphi}(\omega, \mathbf{K})}{\sqrt{\gamma(K,0)}} e^{-i\frac{\omega}{\epsilon}\mathbf{K}\cdot\mathbf{x}_s}, \quad \hat{\varphi}(\omega, \mathbf{K}) = \hat{f}(\omega) - \frac{\gamma(K,0)}{\rho}\mathbf{K}\cdot\hat{\mathbf{F}}(\omega), \tag{A.13}$$

as the amplitude of the incident waves impinging on the layered medium. The up-going wave amplitude $\alpha^\epsilon(\omega, \mathbf{K}, 0^+)$ consists of two parts: the direct arrival, which we remove from the data, and the scattered part

$$\alpha^\epsilon(\omega, \mathbf{K}, 0^-) = \mathcal{R}^\epsilon(\omega, K)\beta^\epsilon(\omega, \mathbf{K}, 0^-), \tag{A.14}$$

where $\mathcal{R}^\epsilon(\omega, K)$ is the reflection coefficient of the layered medium below the surface $z = 0$. The pressure field scattered by the layered structure is obtained by Fourier synthesis:

$$p(t, \vec{\mathbf{x}}) = \frac{\epsilon^{\frac{d+1}{2}}}{2} \int \frac{d\omega}{2\pi\epsilon} \int d\mathbf{K} \left(\frac{\omega}{2\pi\epsilon}\right)^{d-1} \hat{\varphi}(\omega, \mathbf{K})\, \mathcal{R}^\epsilon(\omega, K) e^{-i\frac{\omega}{\epsilon}t + i\frac{\omega}{\epsilon}\mathbf{K}\cdot(\mathbf{x}-\mathbf{x}_s)}, \vec{\mathbf{x}} = (\mathbf{x}, 0). \tag{A.15}$$

It remains to write in the next sections the reflection coefficient $\mathcal{R}^\epsilon(\omega, K)$ in terms of the propagators $\mathbb{P}_j^\epsilon$ of the random slabs and the scattering operators at the interfaces $z = -L_j$ for $j = 1, \ldots, M$.

Similar to (A.15), we obtain by Fourier synthesis the incident field $p^i(t, \vec{\mathbf{y}})$ at a point $\vec{\mathbf{y}}$ in the support $\mathcal{S}$ of the reflectivity (recall Born formula (3.7)). The layered medium appears in $p^i(t, \vec{\mathbf{y}})$ in the form of transmission coefficient $\mathcal{T}^\epsilon(\omega, K)$ between $z = 0$ and $z = -L$, where $\vec{\mathbf{y}} = (\mathbf{y}, -L)$. This transmission coefficient is also determined by the propagators $\mathbb{P}_j^\epsilon$ of the random slabs and the scattering operators at the interfaces $z = -L_j$, for $j = 1, \ldots, M$, as we show in the following sections.

A.3. The Transmission and Reflection Coefficients in the Random Slabs. It follows easily from (A.8) (see [50]) that the propagators $\mathbb{P}_j^\epsilon(\omega, K, z)$ are of the form

$$\mathbb{P}_j^\epsilon = \begin{pmatrix} \zeta_j^\epsilon & \overline{\eta_j^\epsilon} \\ \eta_j^\epsilon & \overline{\zeta_j^\epsilon} \end{pmatrix}, \tag{A.16}$$

where $\zeta_j^\epsilon(\omega, K, z)$ and $\eta_j^\epsilon(\omega, K, z)$ are complex valued fields satisfying

$$\det \mathbb{P}_j^\epsilon(\omega, K, z) = \left|\zeta_j^\epsilon(\omega, K, z)\right|^2 - \left|\eta_j^\epsilon(\omega, K, z)\right|^2 = 1, \quad -L_j < z < -L_{j-1}. \tag{A.17}$$

The bar stands for complex conjugate.

It is not convenient to work directly with the entries of $\mathbb{P}_j^\epsilon$, so we introduce instead the "transmission" and "reflection" coefficients $T_j^\epsilon(\omega, K, z)$ and $R_j^\epsilon(\omega, K, z)$:

$$\mathbb{P}_j^\epsilon(\omega, K, z) \begin{pmatrix} 0 \\ T_j^\epsilon(\omega, K, z) \end{pmatrix} = \begin{pmatrix} R_j^\epsilon(\omega, K, z) \\ 1 \end{pmatrix}. \tag{A.18}$$

This definition can be understood as follows: Imagine that we had a random slab in the interval $(-L_j, z)$ and homogeneous half spaces above and below it, as shown in

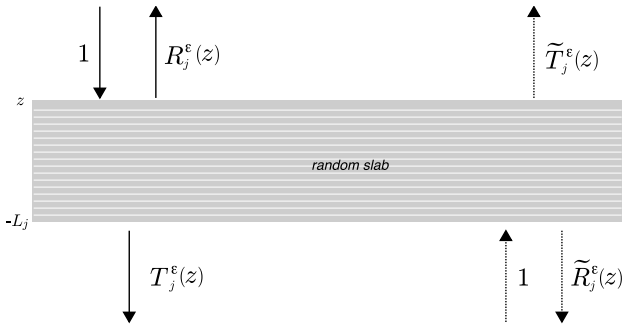

Fig. A.1 *Schematic of transmission and reflection by an imaginary random slab in the interval $(-L_j, z)$, with homogeneous half spaces above and below it. We show on the left the illumination of the slab from above. The illumination from below the slab is shown on the right.*

Figure A.1. Then if we sent a down-going wave of amplitude 1 at z, we would observe a down-going transmitted field $T_j^\epsilon(\omega, K, z)$ at $-L_j$ and a reflected up-going field of amplitude $R_j^\epsilon(\omega, K, z)$ at z. There would be no up-going field at $-L_j$, because there is no scattering below the imaginary slab.

Equations (A.16) and (A.18) give $T_j^\epsilon(\omega, K, z) = \frac{1}{\zeta_j^\epsilon(\omega,K,z)}$, $R_j^\epsilon(\omega, K, z) = \frac{\overline{\eta_j^\epsilon(\omega,K,z)}}{\zeta_j^\epsilon(\omega,K,z)}$, and by (A.17), we have the conservation of energy identity

$$\left|T_j^\epsilon(\omega, K, z)\right|^2 + \left|R_j^\epsilon(\omega, K, z)\right|^2 = 1. \tag{A.19}$$

This holds for any z in the interval $(-L_j, -L_{j-1})$, where $j = 1, \ldots, M$.

We can also define the analogous coefficients $\tilde{T}_j^\epsilon(\omega, K, z)$ and $\tilde{R}_j^\epsilon(\omega, K, z)$ corresponding to illuminating the imaginary random slab from below (see Figure A.1):

$$\mathbb{P}_j^\epsilon(\omega, K, z) \begin{pmatrix} 1 \\ \tilde{R}_j^\epsilon(\omega, K, z) \end{pmatrix} = \begin{pmatrix} \tilde{T}_j^\epsilon(\omega, K, z) \\ 0 \end{pmatrix}. \tag{A.20}$$

These coefficients are given by $\tilde{T}_j^\epsilon(\omega, K, z) = T_j^\epsilon(\omega, K)$ and $\tilde{R}_j^\epsilon(\omega, K, z) = -\frac{\eta_j^\epsilon(\omega,K,z)}{\overline{\zeta_j^\epsilon(\omega,K,z)}}$. They also satisfy the energy conservation identity

$$\left|\tilde{T}_j^\epsilon(\omega, K, z)\right|^2 + \left|\tilde{R}_j^\epsilon(\omega, K, z)\right|^2 = 1. \tag{A.21}$$

The random transmission and reflection coefficients are completely understood, in the sense of their statistical distribution, in the limit $\epsilon \to 0$ [50, 5]. In this paper we need just a few facts about the moments of these coefficients, which we quote from [50, 5]:

(1) The transmission and reflection coefficients of different random slabs (i.e., for different indices j) are statistically independent.

(2) Let z be fixed and consider $\mathcal{U}_{lq}(\omega, K, z) = \left[T_j^\epsilon(\omega, K, z)\right]^l \left[R_j^\epsilon(\omega, K, z)\right]^q$ for arbitrary and nonnegative integers l, q. We have

$$E\left\{\mathcal{U}_{lq}(\omega, K, z)\overline{\mathcal{U}_{l'q'}(\omega', K', z)}\right\} \to 0, \tag{A.22}$$

if $q \neq q'$ or if $q = q' \geq 1$ and $|\omega - \omega'| > O(\epsilon)$, or $|K - K'| > O(\epsilon)$. A similar result holds for $\tilde{R}_j^\epsilon(\omega, K, z)$ replacing $R_j^\epsilon(\omega, K, z)$.

(3) The multifrequency and slowness moments of the transmission coefficients do not vanish,

$$E\left\{\prod_{q\geq 1} T_j^{\epsilon}(\omega_q, K_q, z)\right\} \to E\left\{\prod_{q\geq 1} T_j^{\rm ODA}(\omega_q, K_q, z)\right\}, \tag{A.23}$$

and converge to the moments of the ODA kernel

$$T_j^{\rm ODA}(\omega, K, z) = \exp\left\{-\frac{\omega^2 l}{8}\int_{-L_j}^{z} \frac{ds}{c^2(s)[1-c^2(s)K^2]} + i\frac{\omega\sqrt{l}}{2}\int_{-L_j}^{z} \frac{dW(s+L_j)}{c(s)\sqrt{1-c^2(s)K^2}}\right\}. \tag{A.24}$$

Here W is standard Brownian motion and $l = \ell/\epsilon^2 = O(1)$ is the rescaled correlation length.

A.4. The Strong Scattering Interfaces. We model scattering at the interfaces $-L_j$ with propagators $\mathbb{L}_j$ that map the up- and down-going waves below the interface to those above it.

If the interface is due to a jump discontinuity of $c(z)$ at $-L_j$, we have

$$\begin{pmatrix} \hat{\alpha}^{\epsilon}(\omega, \mathbf{K}, -L_j^+) e^{i\frac{\omega}{\epsilon}\tau_j(K,-L_j)} \\ \hat{\beta}^{\epsilon}(\omega, \mathbf{K}, -L_j^+) e^{-i\frac{\omega}{\epsilon}\tau_j(K,-L_j)} \end{pmatrix} = \mathbb{L}_j(\omega, \mathbf{K}) \begin{pmatrix} \hat{\alpha}^{\epsilon}(\omega, \mathbf{K}, -L_j^-) \\ \hat{\beta}^{\epsilon}(\omega, \mathbf{K}, -L_j^-) \end{pmatrix}, \tag{A.25}$$

where we use $\tau_j(K, -L_j)$ on the left-hand side to increment the travel times (A.7) that start from zero in each random slab. The entries in $\mathbb{L}_j$ are given by [50]

$$\mathbb{L}_j = \begin{pmatrix} \frac{1}{2}\left(\frac{c_j^+}{c_j^-} + \frac{c_j^-}{c_j^+}\right) & -\frac{1}{2}\left(\frac{c_j^+}{c_j^-} - \frac{c_j^-}{c_j^+}\right) \\ -\frac{1}{2}\left(\frac{c_j^+}{c_j^-} - \frac{c_j^-}{c_j^+}\right) & \frac{1}{2}\left(\frac{c_j^+}{c_j^-} + \frac{c_j^-}{c_j^+}\right) \end{pmatrix}, \quad c_j^{\pm} = \frac{c(-L_j^{\pm})}{\sqrt{1-c^2(-L_j^{\pm})K^2}}, \tag{A.26}$$

and we can define, as in section A.3, the transmission and reflection coefficients

$$\mathbb{L}_j \begin{pmatrix} 0 \\ T_j \end{pmatrix} = \begin{pmatrix} R_j \\ 1 \end{pmatrix}, \quad \mathbb{L}_j \begin{pmatrix} 1 \\ \tilde{R}_j \end{pmatrix} = \begin{pmatrix} \tilde{T}_j \\ 0 \end{pmatrix} \tag{A.27}$$

corresponding to illuminations from above and below the interface. They satisfy the identities

$$\tilde{T}_j = T_j, \quad \tilde{R}_j = -R_j, \quad T_j^2 + R_j^2 = 1. \tag{A.28}$$

An alternative model of a strong scattering interface at $-L_j$ is given by a sudden blip of $c(z)$ over a depth interval $-L_j - O(\lambda_o) \leq z \leq -L_j$. We can model such a blip as a perturbation of a constant speed

$$c(z) = c(-L_j^+)\left[1 + \sigma_j \chi\left(\frac{z+L_j}{\epsilon}\right)\right], \quad -\epsilon d_\chi \leq z + L_j \leq 0, \tag{A.29}$$

using a window function $\chi(\xi)$ supported in the $O(1)$ interval $\xi \in [-d_\chi, 0]$. We normalize χ to have maximum value 1, and we let $\sigma_j = O(1)$ be the relative amplitude of the perturbation in (A.29).

If χ were the indicator function of the interval $[-d_\chi, 0]$, the propagator $\mathbb{L}_j$ would be

$$\mathbb{L}_j = \begin{pmatrix} \frac{1}{2}\left(\frac{c_j^+}{c_j^-} + \frac{c_j^-}{c_j^+}\right) & -\frac{1}{2}\left(\frac{c_j^+}{c_j^-} - \frac{c_j^-}{c_j^+}\right) \\ -\frac{1}{2}\left(\frac{c_j^+}{c_j^-} - \frac{c_j^-}{c_j^+}\right) & \frac{1}{2}\left(\frac{c_j^+}{c_j^-} + \frac{c_j^-}{c_j^+}\right) \end{pmatrix} \begin{pmatrix} e^{i\omega d_\chi/c_j^-} & 0 \\ 0 & e^{-i\omega d_\chi/c_j^-} \end{pmatrix}$$
$$\times \begin{pmatrix} \frac{1}{2}\left(\frac{c_j^-}{c_j^+} + \frac{c_j^+}{c_j^-}\right) & -\frac{1}{2}\left(\frac{c_j^-}{c_j^+} - \frac{c_j^+}{c_j^-}\right) \\ -\frac{1}{2}\left(\frac{c_j^-}{c_j^+} - \frac{c_j^+}{c_j^-}\right) & \frac{1}{2}\left(\frac{c_j^-}{c_j^+} + \frac{c_j^+}{c_j^-}\right) \end{pmatrix}.$$

Here $c_j^\pm$ are as in (A.26), with $c(-L_j^-) = c(-L_j^+)(1+\sigma_j)$ and $\mathbb{L}_j$ determined by the product of two matrices of the form (A.26), accounting for the jump discontinuities at $-L_j$ and $-L_j - \epsilon d_\chi$. The travel time $-\epsilon d_\chi/c_j^-$, over the support ϵd_χ of the perturbation of c, appears in $\mathbb{L}_j$ as well. It is easy to check that this complex valued propagator satisfies the analogue of conditions (A.16), (A.17). The transmission and reflection coefficients are defined just as in (A.27), and they satisfy the energy conservation identity

$$|T_j|^2 + |R_j|^2 = 1,$$

which is a consequence of $\det \mathbb{L}_j = 1$.

In the case of a smooth χ, we can obtain the propagator $\mathbb{L}_j$ from (A.8), as follows. Let $z = -L_j + \epsilon\xi$, with $\xi \in [-d_\chi, 0]$, and write the analogue of (A.8) for the propagator $\mathcal{P}_j^\epsilon(\xi)$,

$$\frac{\partial \mathcal{P}_j^\epsilon}{\partial \xi} = \left[i\omega\mu_j\left(\frac{\xi}{\epsilon}\right)\frac{\gamma_j(K,\xi)}{2\rho c_j^2(K,\xi)}\mathbb{H}_j + \frac{\partial}{\partial\xi}\ln\sqrt{\gamma_j(K,\xi)}\,\mathbb{M}_j\right]\mathcal{P}_j^\epsilon,$$
$$\mathcal{P}_j^\epsilon = I \quad \text{at } \xi = -d_\chi. \tag{A.30}$$

Here we use the short notation

$$\mu_j\left(\frac{\xi}{\epsilon}\right) = \mu\left(-\frac{L_j}{\epsilon^2} + \frac{\xi}{\epsilon}\right), \quad \gamma_j(K,\xi) = \rho c_j(K,\xi),$$
$$c_j(K,\xi) = \frac{c(-L_j^+)[1+\sigma_j\chi(\xi)]}{\sqrt{1 - c^2(-L_j^+)[1+\sigma_j\chi(\xi)]^2K^2}},$$

and we define the matrices

$$\mathbb{H}_j = \begin{pmatrix} 1 & -e^{-\frac{2i\omega\xi}{c_j(K,\xi)}} \\ e^{\frac{2i\omega\xi}{c_j(K,\xi)}} & -1 \end{pmatrix}, \qquad \mathbb{M}_j = \begin{pmatrix} 0 & e^{-\frac{2i\omega\xi}{c_j(K,\xi)}} \\ e^{\frac{2i\omega\xi}{c_j(K,\xi)}} & 0 \end{pmatrix}.$$

The propagator $\mathbb{L}_j$ is given by the limit $\epsilon \to 0$ of the solution of (A.30), evaluated at $\xi = 0$. The limit follows from a well-known averaging theorem (see [50, section 6.4.1]), and we obtain

$$\mathbb{L}_j = \mathcal{P}_j(0), \tag{A.31}$$

where

$$\frac{\partial \mathcal{P}_j}{\partial \xi} = \frac{\partial}{\partial \xi} \ln \sqrt{\gamma_j(K,\xi)}\, \mathbb{M}_j \mathcal{P}_j,$$
$$\mathcal{P}_j = I \quad \text{at } \xi = -d_\chi. \tag{A.32}$$

Finally, we define the transmission and reflection coefficients just as in (A.27) and check that they satisfy the energy conservation identity $|T_j|^2 + |R_j|^2 = 1$.

A.5. The Scattering Series. Let us call $-\mathcal{L}$ the maximum depth of propagation of the waves in a bounded and fixed time window. Then, we can use the causality of the wave equation to set the speed $c(z)$ to the constant value $c(-\mathcal{L})$ for $z \le -\mathcal{L}$. Let us also denote by $\mathcal{R}^\epsilon(\omega, K)$ and $\mathcal{T}^\epsilon(\omega, K)$ the reflection and transmission coefficients of the layered medium in the interval $(0, -\mathcal{L})$, at scaled frequency ω and slowness $\mathbf{K}$, with $K = |\mathbf{K}|$. We obtain by iterating (A.9) and (A.25) that

$$\begin{pmatrix} \mathcal{R}^\epsilon(\omega,K) \\ 1 \end{pmatrix} = \mathbb{P}_1^\epsilon(\omega, K, -L_1)\, \mathrm{diag}\left(e^{-i\frac{\omega}{\epsilon}\tau_1(K,-L_1)}, e^{i\frac{\omega}{\epsilon}\tau_1(K,-L_1)}\right) \mathbb{L}_1 \mathbb{P}_2^\epsilon(\omega, K, -L_2) \cdots$$
$$\mathrm{diag}\left(e^{-i\frac{\omega}{\epsilon}\tau_M(K,-L_M)}, e^{i\frac{\omega}{\epsilon}\tau_M(K,-L_M)}\right) \mathbb{L}_M \mathbb{P}_{M+1}^\epsilon(\omega, K, -\mathcal{L}) \begin{pmatrix} 0 \\ \mathcal{T}^\epsilon(\omega,K) \end{pmatrix}. \tag{A.33}$$

Here we assume that there are M strong scattering interfaces above $z = -\mathcal{L}$ and, due to the perfect matching at $z = -\mathcal{L}$, we have no up-going wave coming from the homogeneous half space $z < -\mathcal{L}$.

Equations (A.33) define implicitly $\mathcal{R}^\epsilon$ and $\mathcal{T}^\epsilon$. We invert them next to obtain the scattering series. Note that from now on we use the following simplified notation:

$$\alpha_j^{\epsilon,+} = \alpha_j^\epsilon(\omega, \mathbf{K}, -L_j^+), \quad \beta_j^{\epsilon,+} = \beta_j^\epsilon(\omega, \mathbf{K}, -L_j^+),$$

and similarly for $z = -L_j^-$. We also let $T_j^\epsilon = T_j^\epsilon(\omega, K, -L_{j-1})$, $R_j^\epsilon = R_j^\epsilon(\omega, K, -L_{j-1})$, and $\tau_j = \tau_j(K, -L_j)$.

A.5.1. The Series for $\mathcal{R}^\epsilon$. Let us begin with (A.9). We have

$$\begin{pmatrix} \alpha_{j-1}^{\epsilon,-} \\ \beta_{j-1}^{\epsilon,-} \end{pmatrix} = \mathbb{P}_j^\epsilon \begin{pmatrix} \alpha_j^{\epsilon,+} \\ \beta_j^{\epsilon,+} \end{pmatrix} = \alpha_j^{\epsilon,+} \mathbb{P}_j^\epsilon \begin{pmatrix} 1 \\ \tilde{R}_j^\epsilon \end{pmatrix} + \frac{(\beta_j^{\epsilon,+} - \tilde{R}_j^\epsilon \alpha_j^{\epsilon,+})}{T_j^\epsilon} \mathbb{P}_j^\epsilon \begin{pmatrix} 0 \\ T_j^\epsilon \end{pmatrix},$$

and from definitions (A.18) and (A.20), we get

$$\begin{pmatrix} \alpha_{j-1}^{\epsilon,-} \\ \beta_{j-1}^{\epsilon,-} \end{pmatrix} = \alpha_j^{\epsilon,+} \begin{pmatrix} \tilde{T}_j^\epsilon - R_j^\epsilon \tilde{R}_j^\epsilon / T_j^\epsilon \\ -\tilde{R}_j^\epsilon / T_j^\epsilon \end{pmatrix} + \beta_j^{\epsilon,+} \begin{pmatrix} R_j^\epsilon / T_j^\epsilon \\ 1/T_j^\epsilon \end{pmatrix} \tag{A.34}$$

for $j = 1, \ldots, M+1$. Similarly, we obtain from (A.25) that at $z = -L_j$

$$\begin{pmatrix} \alpha_j^{\epsilon,+} e^{i\frac{\omega}{\epsilon}\tau_j} \\ \beta_j^{\epsilon,+} e^{-i\frac{\omega}{\epsilon}\tau_j} \end{pmatrix} = \alpha_j^{\epsilon,-} \begin{pmatrix} \tilde{T}_j - R_j \tilde{R}_j / T_j \\ -\tilde{R}_j / T_j \end{pmatrix} + \beta_j^{\epsilon,-} \begin{pmatrix} R_j / T_j \\ 1/T_j \end{pmatrix} \tag{A.35}$$

for $j = 1, \ldots, M$. The boundary conditions are

$$\alpha_0^{\epsilon,-} = \mathcal{R}^\epsilon, \quad \beta_0^{\epsilon,-} = 1, \quad \alpha_{M+1}^{\epsilon,+} = 0, \quad \beta_{M+1}^{\epsilon,+} = \mathcal{T}^\epsilon, \tag{A.36}$$

and we set $L_{M+1} = \mathcal{L}$.

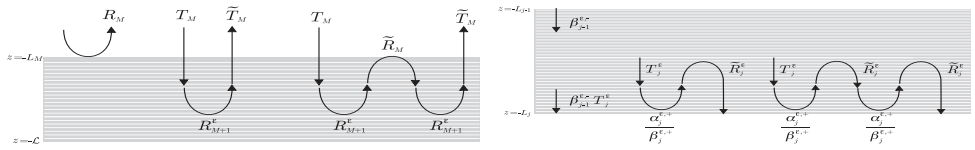

Fig. A.2 *Diagram of the first few terms in the series* (A.38) *on the left and series* (A.41) *on the right.*

Let us start from the bottom in (A.34)–(A.36),

$$\mathcal{T}^\epsilon = \beta_M^{\epsilon,-} T_{M+1}^\epsilon, \quad \frac{\alpha_M^{\epsilon,-}}{\beta_M^{\epsilon,-}} = R_{M+1}^\epsilon, \tag{A.37}$$

and use (A.37) in (A.35) for $j = M$ to get

$$\begin{aligned}\frac{\alpha_M^{\epsilon,+}}{\beta_M^{\epsilon,+}} &= e^{-2i\frac{\omega}{\epsilon}\tau_M}\left(\frac{\alpha_M^{\epsilon,-}(\tilde{T}_M - R_M\tilde{R}_M/T_M) + \beta_M^{\epsilon,-}R_M/T_M}{\beta_M^{\epsilon,-}/T_M - \alpha_M^{\epsilon,-}\tilde{R}_M/T_M}\right)\\ &= e^{-2i\frac{\omega}{\epsilon}\tau_M}\left(R_M + \frac{R_{M+1}^\epsilon T_M\tilde{T}_M}{1-\tilde{R}_M R_{M+1}^\epsilon}\right).\end{aligned}$$

Since the reflection coefficients are less than 1 in magnitude, we obtain

$$\frac{\alpha_M^{\epsilon,+}}{\beta_M^{\epsilon,+}} = e^{-2i\frac{\omega}{\epsilon}\tau_M}\left[R_M + R_{M+1}^\epsilon T_M\tilde{T}_M\sum_{q=0}^{\infty}\left(\tilde{R}_M R_{M+1}^\epsilon\right)^q\right]. \tag{A.38}$$

This series says that, as indicated in the diagram in Figure A.2, the reflected field at $-L_M^+$ consists of the following: (1) the direct reflection at the interface $z = -L_M$ (R_M in (A.38)); (2) the transmission through the interface and the reflection by the medium below, followed by another transmission from below the interface ($T_M R_{M+1}^\epsilon \tilde{T}_M$ in (A.38)); (3) multiple iterations of the latter. Due to reflections at $-L_M$, we have multiple illuminations of the medium below $z = -L_M$. These are terms $T_M(\tilde{R}_M R_{M+1}^\epsilon)^q R_{M+1}^\epsilon \tilde{T}_M$ for $q > 0$ in (A.38).

The series for $\frac{\alpha_{M-1}^{\epsilon,-}}{\beta_{M-1}^{\epsilon,-}}$ is obtained in an analogous manner:

$$\frac{\alpha_{M-1}^{\epsilon,-}}{\beta_{M-1}^{\epsilon,-}} = R_M^\epsilon + \frac{\alpha_M^{\epsilon,+}}{\beta_M^{\epsilon,+}} T_M^\epsilon \tilde{T}_M^\epsilon \sum_{q=0}^{\infty}\left(\tilde{R}_M^\epsilon \frac{\alpha_M^{\epsilon,+}}{\beta_M^{\epsilon,+}}\right)^q.$$

Iterating for all indices j, we obtain the full scattering series

$$\frac{\alpha_j^{\epsilon,+}}{\beta_j^{\epsilon,+}} = e^{-2i\frac{\omega}{\epsilon}\tau_j}\left[R_j + \frac{\alpha_j^{\epsilon,-}}{\beta_j^{\epsilon,-}} T_j\tilde{T}_j\sum_{q=0}^{\infty}\left(\tilde{R}_j\frac{\alpha_j^{\epsilon,-}}{\beta_j^{\epsilon,-}}\right)^q\right], \tag{A.39}$$

where $j = 1, \ldots, M$. At $j = M$ we have (A.37) and

$$\frac{\alpha_{j-1}^{\epsilon,-}}{\beta_{j-1}^{\epsilon,-}} = R_j^\epsilon + \frac{\alpha_j^{\epsilon,+}}{\beta_j^{\epsilon,+}} T_j^\epsilon \tilde{T}_j^\epsilon \sum_{q=0}^{\infty}\left(\tilde{R}_j^\epsilon \frac{\alpha_j^{\epsilon,+}}{\beta_j^{\epsilon,+}}\right)^q, \quad j = 1, \ldots, M. \tag{A.40}$$

Finally, (A.36) gives $\mathcal{R}^\epsilon = \frac{\alpha_0^{\epsilon,-}}{\beta_0^{\epsilon,-}}$.

A.5.2. The Series for $\mathcal{T}^\epsilon$. The derivation of the series for $\mathcal{T}^\epsilon$ is analogous to that for $\mathcal{R}^\epsilon$. We directly state the result here: For $j = 1, \ldots, M$, we have

$$\beta_j^{\epsilon,+} = \beta_{j-1}^{\epsilon,-} T_j^\epsilon \sum_{q=0}^{\infty} \left(\tilde{R}_j^\epsilon \frac{\alpha_j^{\epsilon,+}}{\beta_j^{\epsilon,+}} \right)^q \tag{A.41}$$

and

$$\beta_j^{\epsilon,-} = \beta_j^{\epsilon,+} e^{-i\frac{\omega}{\epsilon}\tau_j} T_j \sum_{q=0}^{\infty} \left(\tilde{R}_j \frac{\alpha_j^{\epsilon,-}}{\beta_j^{\epsilon,-}} \right)^q . \tag{A.42}$$

The first terms in (A.41) and (A.42) are the direct transmission through the jth random slab and interface, respectively. The series arise because of the multiple illuminations of the slab and interface, due to the reflection by the layered structure below $-L_j$. See, for example, the diagram in Figure A.2 for series (A.41). At $z = 0$ we have the initial condition (A.13) and $\mathcal{T}^\epsilon = \beta_{M+1}^{\epsilon,+}$.

A.6. The Scattered Pressure Field. Assume first times $t < \tau^{\mathcal{S}}$, so that all the echoes at the array are due to the layered structure. The pressure field at the receivers is given by (A.15), in terms of the reflection coefficient $\mathcal{R}^\epsilon$ defined by the scattering series derived in section A.5.1. The series involves random reflection and transmission coefficients T_j^ϵ and R_j^ϵ, with moments given in section A.3, in the asymptotic limit $\epsilon \to 0$.

Note in particular statements (A.22) and (A.23). They say that when computing the expectation of $p(t, \vec{\mathbf{x}})$, we can drop all terms in $\mathcal{R}^\epsilon$ that involve reflections by the random slabs and replace the transmission coefficients T_j^ϵ by the ODA kernels T_j^{ODA}. That is, we can write

$$E\left\{p(t, \vec{\mathbf{x}})\right\} \approx E\left\{p^{\mathrm{ODA}}(t, \vec{\mathbf{x}})\right\}, \tag{A.43}$$

where $\vec{\mathbf{x}} = (\mathbf{x}, 0)$,

$$p^{\mathrm{ODA}}(t, \vec{\mathbf{x}}) = \frac{\epsilon^{\frac{d+1}{2}}}{2} \int \frac{d\omega}{2\pi\epsilon} \int d\mathbf{K} \left(\frac{\omega}{2\pi\epsilon} \right)^{d-1} \hat{\varphi}(\omega, \mathbf{K})\, \mathcal{R}^{\mathrm{ODA}}(\omega, K) e^{-i\frac{\omega}{\epsilon}t + i\frac{\omega}{\epsilon}\mathbf{K}\cdot(\mathbf{x}-\mathbf{x}_s)}, \tag{A.44}$$

and $\mathcal{R}^{\mathrm{ODA}} = \frac{\alpha_0^{\mathrm{ODA},-}}{\beta_0^{\mathrm{ODA},-}}$ is determined recursively from

$$\begin{aligned}
&\frac{\alpha_j^{\mathrm{ODA},+}}{\beta_j^{\mathrm{ODA},+}} = e^{-2i\frac{\omega}{\epsilon}\tau_j} \left[R_j + \frac{\alpha_j^{\mathrm{ODA},-}}{\beta_j^{\mathrm{ODA},-}} T_j \tilde{T}_j \sum_{q=0}^{\infty} \left(\tilde{R}_j \frac{\alpha_j^{\mathrm{ODA},-}}{\beta_j^{\mathrm{ODA},-}} \right)^q \right], \\
&\frac{\alpha_{j-1}^{\mathrm{ODA},-}}{\beta_{j-1}^{\mathrm{ODA},-}} = \frac{\alpha_j^{\mathrm{ODA},+}}{\beta_j^{\mathrm{ODA},+}} \left[T_j^{\mathrm{ODA}} \right]^2, \quad j = 1, \ldots, M, \\
&\frac{\alpha_M^{\mathrm{ODA},-}}{\beta_M^{\mathrm{ODA},-}} = 0.
\end{aligned} \tag{A.45}$$

Furthermore, due to the rapid decorrelation of the reflection coefficients R_j^ϵ over frequencies and slownesses K, we get from (A.15) and (A.22) that

$$E\left\{ \left| p(t, \vec{\mathbf{x}}) \right|^2 \right\} = E\left\{ \left| p^{\mathrm{ODA}}(t, \vec{\mathbf{x}}) \right|^2 \right\} + O(\epsilon). \tag{A.46}$$

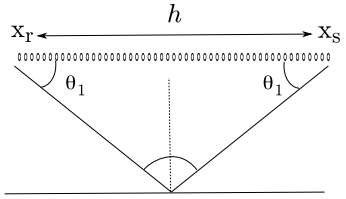

Fig. A.3 *Diagram of Snell's law for reflection at $z = -L_1$.*

The ODA field (A.44) describes the coherent echoes recorded at the array. They are due to scattering by the strong interfaces at $z = -L_j$, for $j = 1, \ldots, M$, but not to scattering in the random medium. Scattering in the random medium produces what we call the incoherent field. It has zero expectation and $O(\epsilon)$ variance (see the second term in (A.46)). The coherent field $p^{\rm ODA}(t, \vec{\mathbf{x}})$ consists of a series of coherent arrivals along scattering paths that we denote in short by $\mathcal{P}$. Each such arrival can be analyzed with the method of stationary phase [20].

Take, for example, the shortest path $\mathcal{P}$, corresponding to a single reflection at $-L_1$, and assume for the purpose of illustration that $c(z) = c_o$ and $d = 3$. We have

$$p^{\rm ODA}_{\mathcal{P}}(t, \vec{\mathbf{x}}) = \frac{\epsilon^2}{2} \int \frac{d\omega}{2\pi\epsilon} \int d\mathbf{K} \left(\frac{\omega}{2\pi\epsilon}\right)^2 \hat{\varphi}(\omega, \mathbf{K})\, R_1 \left[T_1^{\rm ODA}(\omega, K)\right]^2 e^{-i\frac{\omega}{\epsilon}(t+2\tau_1)+i\frac{\omega}{\epsilon}\mathbf{K}\cdot(\mathbf{x}-\mathbf{x}_s)},$$

with kernel $T_1^{\rm ODA}(\omega, K)$ given by (A.24), for $j = 1$ and $z = 0$. The travel time is

$$\tau_1 = -L_1 \frac{\sqrt{1 - c_o^2 K^2}}{c_o}$$

and

$$T_1^{\rm ODA}(\omega, K) = \exp\left\{ -\frac{\omega^2 l L_1}{8c_o^2(1 - c_o^2K^2)} + i\frac{\omega\sqrt{l}}{2c_o\sqrt{1 - c_o^2K^2}} W(L_1) \right\}.$$

The leading term in the integral over $\mathbf{K}$ comes from the neighborhood of the stationary point

$$\mathbf{K} = \frac{\mathbf{h}}{c_o\sqrt{|\mathbf{h}|^2 + 4L_1^2}}, \quad K = |\mathbf{K}| = \frac{\cos\theta_1}{c_o}.$$

This corresponds to waves propagating along a straight path from the array to the interface at $-L_1$ and back. The reflection at $-L_1$ obeys Snell's law, as indicated in Figure A.3. A straightforward application of stationary phase gives

$$p^{\rm ODA}_{\mathcal{P}}(t, \vec{\mathbf{x}}) = \frac{\epsilon}{4\pi\sqrt{h^2 + 4L_1^2}} \int \frac{d\omega}{2\pi} \left(-i\frac{\omega}{\epsilon}\frac{\sin\theta_1}{c_o}\right) \times \left(\hat{f}(\omega) - \frac{\mathbf{h}\cdot\hat{\mathbf{F}}(\omega)}{2L_1}\right) R_1 e^{-\frac{\omega^2 t_{\rm ps}^2}{\sin^2\theta_1} + 2i\frac{\omega t_{\rm ps}}{\sin\theta_1}\frac{W(L_1)}{\sqrt{L_1}} - i\frac{\omega}{\epsilon}\left(t - \frac{\sqrt{|\mathbf{h}|^2+4L_1^2}}{c_o}\right)}.$$

This result is similar to (3.25). It says that the coherent echo along path $\mathcal{P}$ looks as if we had a homogeneous medium, except for the following: (1) the pulse spread

controlled by parameter

$$t_{\rm ps} = \frac{\sqrt{lL_1}}{2c_o}$$

with units of time, and (2) the random arrival shift $\epsilon\delta\tau_{\mathcal{P}}$, with

$$\delta\tau_{\mathcal{P}} = \frac{2t_{\rm ps}}{\sin\theta_1}\frac{W(L_1)}{\sqrt{L_1}}.$$

Obviously, the above illustration extends to all the coherent paths and to variable, but smooth $c(z)$. Consistent with the notation in (3.22), we denote the pulse shape for each coherent arrival by

$$\Phi_{\mathcal{P}}\left[\frac{t-\tau_{\mathcal{P}}(\mathbf{h})-\epsilon\delta\tau_{\mathcal{P}}(\mathbf{h})}{\epsilon},\mathbf{h}\right].$$

We use the second argument to point out that $\Phi_{\mathcal{P}}$ changes with $\mathbf{h}$. This is a slow change due to geometrical spreading and the convolution with the ODA kernel. The rapid variation with $\mathbf{h}$ is due to the travel time $\tau_{\mathcal{P}}(\mathbf{h})$ in the first argument of $\Phi_{\mathcal{P}}$.

Finally, let us point out that the results in this section extend obviously to the echoes from the reflectivity support $\mathcal{S}$ using the series derived in section A.5.2 for $\mathcal{T}^{\epsilon}$ and the Born approximation.

REFERENCES

[1] R. Adler and J. Taylor, *Random Fields and Geometry*, Springer, New York, 2007.

[2] R. Alonso, L. Borcea, G. Papanicolaou, and C. Tsogka, *Detection and imaging in strongly backscattering randomly layered media*, Inverse Problems, 27 (2011), 025004.

[3] H. Ammari, J. Garnier, and K. Sølna, *A statistical approach to target detection and localization in the presence of noise*, Waves Random Complex Media, 22 (2012), pp. 40–65.

[4] S. Arridge and J. Schotland, *Optical Tomography: Forward and Inverse Problems*, Inverse Problems, 25 (2009), 123010.

[5] M. Asch, W. Kohler, G. Papanicolaou, M. Postel, and B. White, *Frequency content of randomly scattered signals*, SIAM Rev., 33 (1991), pp. 519–625.

[6] A. Aubry and A. Derode, *Random matrix theory applied to acoustic backscattering and imaging in complex media*, Phys. Rev. Lett., 102 (2009), 084301.

[7] A. Aubry and A. Derode, *Singular value distribution of the propagation matrix in random scattering media*, Waves Random Complex Media, 20 (2010), pp. 333–363.

[8] A. Aubry and A. Derode, *Detection and imaging in a random medium: A matrix method to overcome multiple scattering and aberration*, J. Appl. Phys., 106 (2009), 044903.

[9] J. Baik, G. Ben Arous, and S. Péché, *Phase transition of the largest eigenvalue for nonnull complex sample covariance matrices*, Ann. Probab., 33 (2005), pp. 1643–1697.

[10] J. Baik, R. Buckingham, and J. DiFranco, *Asymptotics of Tracy-Widom distributions and the total integral of a Painlevé* II *function*, Comm. Math. Phys., 280 (2008), pp. 463–497.

[11] A. Bakulin and R. Calvert, *The virtual source method: Theory and case study*, Geophys., 71 (2006), pp. SI139–SI150.

[12] G. Bal and K. Ren, *Transport-based imaging in random media*, SIAM J. Appl. Math., 68 (2008), pp. 1738–1762.

[13] R. Baraniuk and P. Steeghs, *Compressive radar imaging*, in Proceedings of the 2007 IEEE Radar Conference, 2007, pp. 128–133.

[14] E. Bécache, P. Joly, and C. Tsogka, *Étude d'un nouvel élément fini mixte permettant la condensation de masse*, C. R. Acad. Sci. Paris Sér. I Math., 324 (1997), pp. 1281–1286.

[15] E. Bécache, P. Joly, and C. Tsogka, *An analysis of new mixed finite elements for the approximation of wave propagation problems*, SIAM J. Numer. Anal., 37 (2000), pp. 1053–1084.

[16] J. G. Berryman, *Stable iterative reconstruction algorithm for nonlinear traveltime tomography*, Inverse Problems, 6 (1990), pp. 21–43.

[17] G. Beylkin, *Imaging of discontinuities in the inverse scattering problem by inversion of a causal generalized Radon transform*, J. Math. Phys., 26 (1985), pp. 99–108.
[18] G. Beylkin and R. Burridge, *Linearized inverse scattering problem of acoustics and elasticity*, Wave Motion, 12 (1990), pp. 15–22.
[19] B. Biondi, *3D Seismic Imaging*, Investigations in Geophysics 14, Society of Exploration Geophysicists, Tulsa, OK, 2006.
[20] N. Bleistein, J. K. Cohen, and J. W. Stockwell, Jr., *Mathematics of Multidimensional Seismic Imaging, Migration, and Inversion*, Springer, New York, 2001.
[21] E. Bleszynski, M. Bleszynski, T. Jariszewicz, L. Borcea, T. Callaghan, and G. Papanicolaou, *Autofocus and Target Motion Estimation in SAR*, Airforce SBIR Progress Report 2012, contract FA8650-10-C-1705.
[22] P. Blomgren, G. Papanicolaou, and H. Zhao, *Super-resolution in time-reversal acoustics*, J. Acoust. Soc. Amer., 111 (2002), pp. 230–248.
[23] L. Borcea, *Robust interferometric imaging in random media*, in The Radon Transform, Inverse Problems, and Tomography, Proc. Sympos. Appl. Math. 63, AMS, Providence, RI, 2006, pp. 129–156.
[24] L. Borcea, T. Callaghan, J. Garnier, and G. Papanicolaou, *A universal filter for enhanced imaging with small arrays*, Inverse Problems, 26 (2010), 015006.
[25] L. Borcea, T. Callaghan, and G. Papanicolaou, *Synthetic aperture radar imaging with motion estimation and autofocus*, Inverse Problems, 28 (2012), 045006.
[26] L. Borcea, J. Garnier, G. Papanicolaou, and C. Tsogka, *Enhanced statistical stability in coherent interferometric imaging*, Inverse Problems, 27 (2011), 085003.
[27] L. Borcea, F. González del Cueto, G. Papanicolaou, and C. Tsogka, *Filtering random layering effects in imaging*, Multiscale Model. Simul., 8 (2010), pp. 751–781.
[28] L. Borcea, L. Issa, and C. Tsogka, *Source localization in random acoustic waveguides*, Multiscale Model. Simul., 8 (2010), pp. 1981–2022.
[29] L. Borcea, G. Papanicolaou, and F. Guevarra Vasquez, *Edge illumination and imaging of extended reflectors*, SIAM Imaging Sci., 1 (2008), pp. 75–114.
[30] L. Borcea, G. Papanicolaou, and C. Tsogka, *Adaptive interferometric imaging in clutter and optimal illumination*, Inverse Problems, 22 (2006), pp. 1405–1436.
[31] L. Borcea, G. Papanicolaou, and C. Tsogka, *Coherent interferometric imaging in clutter*, Geophysics, 71 (2006), pp. 1165–1175.
[32] L. Borcea, G. Papanicolaou, and C. Tsogka, *Coherent interferometry in finely layered random media*, Multiscale Model. Simul., 5 (2006), pp. 62–83.
[33] L. Borcea, G. Papanicolaou, and C. Tsogka, *Asymptotics for the space-time Wigner transform with applications to imaging*, in Stochastic Differential Equations: Theory and Applications (in Honor of Prof. Boris L. Rozovskii), Interdiscip. Math. Sci. 2, P. H. Baxendale and S. V. Lototsky, eds., World Scientific, Hackensack, NJ, 2007, pp. 91–112.
[34] L. Borcea, G. Papanicolaou, and C. Tsogka, *Optimal illumination and waveform design for imaging in random media*, J. Acoust. Soc. Amer., 122 (2007), pp. 3507–3518.
[35] L. Borcea, G. Papanicolaou, and C. Tsogka, *Adaptive time-frequency detection and filtering for imaging in heavy clutter*, SIAM Imaging Sci., 4 (2011), pp. 827–849.
[36] B. Borden, *Mathematical problems in radar inverse scattering*, Inverse Problems, 19 (2002), pp. R1–R28.
[37] M. Born and E. Wolf, *Principles of Optics*, Cambridge University Press, Cambridge, UK, 1999.
[38] A. Böttcher and B. Silbermann, *Introduction to Large Truncated Toeplitz Matrices*, Springer, New York, 1999.
[39] J. Carazzone and W. Symes, *Velocity inversion by differential semblance optimization*, Geophys., 56 (1991), pp. 654–663.
[40] A. Chai, M. Moscoso, and G. Papanicolaou, *Robust Imaging of Localized Scatterers Using the Singular Value Decomposition and l_1 Minimization*, preprint, http://math.stanford.edu/~papanico/pubs.html#inv.
[41] J. F. Claerbout, *Fundamentals of Geophysical Data Processing: With Applications to Petroleum Prospecting*, Blackwell Scientific, Palo Alto, CA, 1985.
[42] J. F. Claerbout, *Earth Soundings Analysis: Processing versus Inversion*, Blackwell Scientific Publications, Palo Alto, CA, 1992.
[43] J. F. Clouet and J. P. Fouque, *Spreading of a pulse travelling in random media*, Ann. Appl. Probab., 4 (1994), pp. 1083–1097.
[44] J. C. Curlander and R. N. McDonough, *Synthetic Aperture Radar*, Wiley, New York, 1991.
[45] L. Demanet, P. D. Letourneau, N. Boumal, H. Calandra, J. Chiu, and S. Snelson, *Matrix probing: A randomized preconditioner for the wave-equation Hessian*, Appl. Comput. Harmon. Anal., 32 (2012), pp. 155–168

[46] A. Fannjiang, *Exact localization and superresolution with noisy data and random illumination*, Inverse Problems, 27 (2011), 065012
[47] M. Fink, *Time-reversed acoustics*, Sci. Amer., 281 (1999), pp. 91–97.
[48] S. Fomel, *Application of plane-wave destruction filters*, Geophys., 67 (2002), pp. 1946–1960.
[49] S. Fomel, E. Landa, and M. Turham Taner, *Poststack velocity analysis by separation and imaging of seismic diffractors*, Geophys., 72 (2007), pp. U89–U94.
[50] J.-P. Fouque, J. Garnier, G. Papanicolaou, and K. Sølna, *Wave Propagation and Time Reversal in Randomly Layered Media*, Springer, New York, 2007.
[51] J. Garnier, *Use of random matrix theory for target detection, localization, and reconstruction*, Contemp. Math., 548 (2011), pp. 1–19.
[52] J. Garnier and G. Papanicolaou, *Correlation based virtual source imaging in strongly scattering random media*, Inverse Problems, 28 (2012), 075002.
[53] U. Grenander and G. Szegö, *Toeplitz Forms and Their Applications*, California Monogr. Math. Sci. 20, University of California Press, Berkeley, Los Angeles, 1958.
[54] F. Herrmann, P. Moghaddam, and C. Stolk, *Sparsity and continuity promoting seismic image recovery with curvelet frames*, Appl. Comput. Harmon. Anal., 24 (2008), pp. 150–173.
[55] M. Kac, W. L. Murdock, and G. Szegö, *On the eigenvalues of certain Hermitian forms*, J. Ration. Mech. Anal., 2 (1953), pp. 767–800.
[56] S. Mallat, *A Wavelet Tour of Signal Processing*, 2nd ed., Academic Press, San Diego, CA, 1999.
[57] V. A. Marchenko and L. A. Pastur, *Distribution of eigenvalues of some sets of random matrices*, Math. USSR-Sb., 1 (1967), pp. 507–536.
[58] R. Nammour, *Approximate Multi-Parameter Inverse Scattering Using Pseudodifferential Scaling*, Ph.D. thesis, Computational and Applied Mathematics, Rice University, 2011.
[59] R. F. O'Doherty and N. A. Anstey, *Reflections on amplitudes*, Geophys. Prospect., 19 (1971), pp. 430–458.
[60] G. Papanicolaou, L. Ryzhik, and K. Sølna, *Statistical stability in time reversal*, SIAM J. Appl. Math., 64 (2004), pp. 1133–1155.
[61] G. Peyré, *MATLAB Toolbox Fast Marching*, software download from MATLAB Central, http://www.mathworks.com/matlabcentral/.
[62] L. Ryzhik, G. Papanicolaou, and J. B. Keller, *Transport equations for elastic and other waves in random media*, Wave Motion, 24 (1996), pp. 327–370.
[63] G. T. Schuster, *Seismic Interferometry*, Cambridge University Press, Cambridge, UK, 2009.
[64] P. Sheng, *Introduction to Wave Scattering, Localization and Mesoscopic Phenomena*, Academic Press, New York, 1995.
[65] K. Sølna and G. Papanicolaou, *Ray theory for a locally layered random medium*, Waves Random Media, 10 (2000), pp. 151–198.
[66] P. Stefanov and G. Uhlmann, *Recent progress on the boundary rigidity problem*, Electron. Res. Announc. Amer. Math. Soc., 11 (2005), pp. 64–70.
[67] C. C. Stolk, *Microlocal analysis of a seismic linearized inverse problem*, Wave Motion, 32 (2000), pp. 267–290.
[68] W. Symes, *All Stationary Points of Differential Semblance Are Asymptotic Global Minimizers: Layered Acoustics*, Stanford Exploration Project 100, Stanford University, Stanford, CA, 1999, pp. 71–92.
[69] M. C. W. van Rossum and Th. M. Nieuwenhuizen, *Multiple scattering of classical waves: Microscopy, mesoscopy, and diffusion*, Rev. Modern Phys., 71 (1999), pp. 313–371.
[70] K. Wapenaar, E. Slob, R. Snieder, and A. Curtis, *Tutorial on seismic interferometry: Part 2—Underlying theory and new advances*, Geophys., 75 (2010), pp. A211–A227.
[71] B. White, P. Sheng, and B. Nair, *Localization and backscattering spectrum of seismic waves in stratified lithology*, Geophys., 55 (1990), pp. 1158–1165.